The Astrophysical Journal, 941:3 (16pp), 2022 December 10 https://doi.org/10.3847/1538-4357/ac9dfc

First Detection of the Molecular Cloud Population in the Extended Ultraviolet Disk of M83

Jin Koda[1], Linda Watson[2,3], Françoise Combes[4], Monica Rubio[5], Samuel Boissier[6], Masafumi Yagi[7], David Thilker[8], Amanda M Lee[1], Yutaka Komiyama[7,9,10], Kana Morokuma-Matsui[11], and Celia Verdugo[3]
[1] Department of Physics and Astronomy, Stony Brook University, Stony Brook, NY 11794-3800, USA; jin.koda@stonybrook.edu
[2] European Southern Observatory, Germany
[3] Joint ALMA Observatory (JAO), Alonso de Córdova 3107, Vitacura, Santiago, Chile
[4] Observatoire de Paris, LERMA, Collège de France, PSL Univ., CNRS, Sorbonne Univ., Paris, France
[5] Departamento de Astronomia, Universidad de Chile, Casilla 36-D, Santiago, Chile
[6] Aix Marseille Univ., CNRS, CNES, Laboratoire d'Astrophysique de Marseille, Marseille, France
[7] National Astronomical Observatory of Japan, Mitaka, Tokyo 181-8588, Japan
[8] Department of Physics and Astronomy, The Johns Hopkins University, Baltimore, MD 21218, USA
[9] Dept. of Advanced Sciences, Faculty of Science and Engineering, Hosei University, 3-7-2 Kajino-cho, Koganei-shi, Tokyo 184-8584, Japan
[10] Graduate University for Advanced Studies (SOKENDAI), Mitaka, Tokyo 181-8588, Japan
[11] Institute of Astronomy, Graduate School of Science, The University of Tokyo, 2-21-1 Osawa, Mitaka, Tokyo 181-0015, Japan
Received 2022 March 19; revised 2022 September 23; accepted 2022 September 23; published 2022 December 7

Abstract

We report a CO($J = 3-2$) detection of 23 molecular clouds in the extended ultraviolet (XUV) disk of the spiral galaxy M83 with the Atacama Large Millimeter/submillimeter Array. The observed 1 kpc^2 region is at about 1.24 times the optical radius (R_{25}) of the disk, where CO($J = 2$–1) was previously not detected. The detection and nondetection, as well as the level of star formation (SF) activity in the region, can be explained consistently if the clouds have the mass distribution common among Galactic clouds, such as Orion A—with star-forming dense clumps embedded in thick layers of bulk molecular gas, but in a low-metallicity regime where their outer layers are CO-deficient and CO-dark. The cloud and clump masses, estimated from CO(3−2), range from 8.2×10^2 to 2.3×10^4 $M_\odot$ and from 2.7×10^2 to 7.5×10^3 $M_\odot$, respectively. The most massive clouds appear similar to Orion A in star formation activity as well as in mass, as expected if the cloud mass structure is common. The overall low SF activity in the XUV disk could be due to the relative shortage of gas in the molecular phase. The clouds are distributed like chains up to 600 pc (or longer) in length, suggesting that the trigger of cloud formation is on large scales. The common cloud mass structure also justifies the use of high-J CO transitions to trace the total gas mass of clouds, or galaxies, even in the high-z universe. This study is the first demonstration that CO(3−2) is an efficient tracer of molecular clouds even in low-metallicity environments.

Unified Astronomy Thesaurus concepts: Interstellar medium (847); Molecular clouds (1072); Galaxy evolution (594); Star formation (1569); Spiral galaxies (1560)

1. Introduction

The Galaxy Evolution Explorer (GALEX) satellite found massive star formation (SF) in the far outskirts of galactic disks (Gil de Paz et al. 2005; Thilker et al. 2005). Bright ultraviolet (UV) sources are distributed beyond the optical radius R_{25}. They reveal abundant and recent (<100 Myr) SF (Gil de Paz et al. 2005; Thilker et al. 2005; Lemonias et al. 2011, see Figure 1 for the example of M83). These extended UV disks, dubbed extended ultraviolet (XUV) disks, are fairly common among local disk galaxies (Thilker et al. 2007). They offer an opportunity to study SF in extreme conditions, particularly at a low average gas density and molecular fraction. XUV disks often exhibit lower Hα-to-far-UV (FUV) flux ratios than the optical disk, which likely demonstrates the importance of stochastic sampling of the initial mass function (IMF) and/or bursty SF histories in these regions (e.g., Alberts et al. 2011; Koda et al. 2012b; Watson et al. 2016).

Molecular clouds host virtually all SF within the optical disks of local galaxies. It is crucial to study whether the same is true in XUV disks. The Milky Way's outer disk hosts small molecular clouds (10^{2-4} $M_\odot$; Sun et al. 2015, 2017), but unlike XUV disks there is not much SF above late B-type stars (Izumi et al. 2017). Numerous efforts have been made to detect CO emission in XUV disks, but they have rarely succeeded (Watson & Koda 2017, for review including unpublished efforts that resulted in nondetections). Only four galaxies with XUV disks permitted CO detection at a few positions in their outskirts: NGC 4414 (Braine & Herpin 2004), NGC 6946 (Braine et al. 2007), M33 (Braine et al. 2010), and M63 (Dessauges-Zavadsky et al. 2014). Most detections could not reveal individual clouds in the vicinity of UV emission due to low sensitivity and resolution ($\gtrsim 10^{5-6}$ $M_\odot$ and $\gtrsim$300–500 pc). Only M33, the closest to the Milky Way, allowed detection down to $\gtrsim 4 \times 10^4$ $M_\odot$ in two regions beyond the R_{25} radius, and only one of them is identified as a single cloud (Braine et al. 2012). The rarity of the CO detection is at odds with the abundance of the UV sources across the XUV disks.

M83 is at a distance of $D = 4.5$ Mpc (Thim et al. 2003) and is one of the nearest XUV disks. Previous Atacama Large Millimeter/submillimeter Array (ALMA) observations of CO(2−1) in the XUV disk of M83 resulted in nondetection (Bicalho et al. 2019) even at a high sensitivity of 2.2×10^4 $M_\odot$ (3σ; calculated with the low CO-to-H_2 conversion factor in the

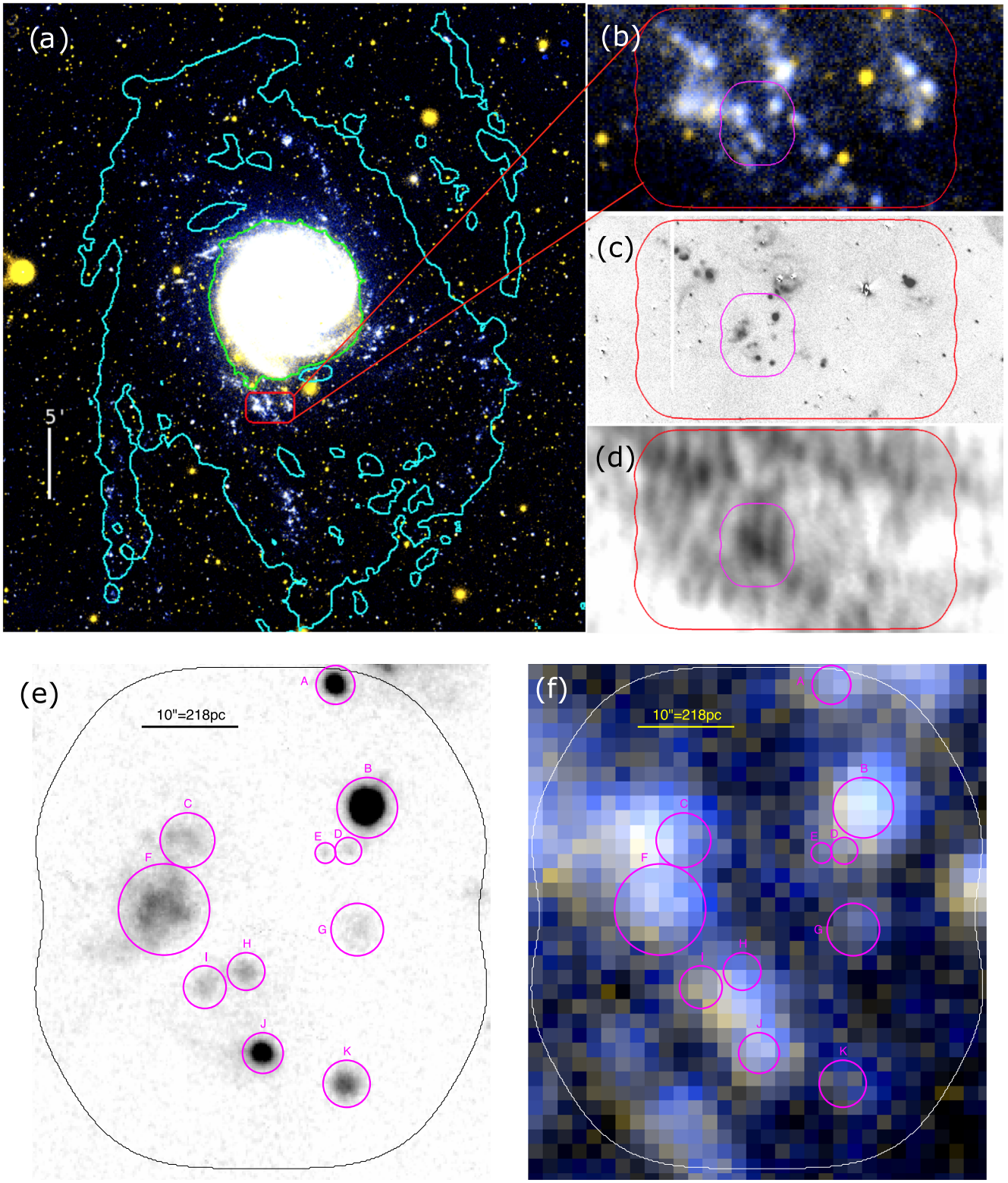

Figure 1. (a) GALEX FUV and NUV-band color composite image. The inner (green) and outer (cyan) contours are the edge of the optical disk and the extent of H I gas at an H I surface density of 1.5×10^{20} cm^{-2} (see Koda et al. 2012b). The red box is the $1\farcm5 \times 3'$ (2.0×3.9 kpc^2) field from the ALMA CO($J = 2$–1) observations (Bicalho et al. 2019). The three panels on the right are zoom-ins to the CO(2−1) field: (b) the GALEX color composite, as in panel (a), (c) the continuum-subtracted Hα image from the Subaru telescope, and (d) the H I 21 cm emission image from Walter et al. (2008). The area of our CO(3−2) observations is indicated by the inner magenta box of $\sim 0\farcm75 \times 0\farcm85$ ($\sim 0.98 \times 1.11$ kpc^2). The bottom two panels are zoom-ins to the CO(3−2) field: (e) the Hα image with visually identified H II regions (circles); (f) the same as (e), but on the GALEX color composite. Panels (e), (f), and Figures 2, 3, and 7 show the same region, and their coordinates are written explicitly in Figures 2 and 3.

Table 1
Parameters of Reduced Data

Data	Bandwidth	Channel Width	Cell Size	Beam Size	Covered Scale	rms (1σ)	
				b_{maj}, b_{min}, PA	min, max		
	(GHz)	(km s^{-1})	(arcsec)	(arcsec, arcsec, deg)	(arcsec, arcsec)	(mJy beam^{-1})	(mK)
CO 3–2		2.54	0.15	0.96, 0.82, −84.7	0.57, 13.7	0.96	12.5
		1.00	0.15	0.96, 0.82, −84.7	0.57, 13.7	1.31	17.0
349 GHz cont.	5.625		0.15	0.95, 0.81, −85.0	0.56, 13.8	0.030	0.39
CO 2–1		2.54	0.15	0.76, 0.55, −88.6	0.49, 10.7	10.6	58
225 GHz cont.	5.625		0.15	0.79, 0.60, −81.9	0.47, 11.1	0.22	12

Large Magellanic Cloud (LMC) from Fukui et al. 2008). The observed field is a relatively large area of $\sim 1\farcm5 \times 3'$ (2×4 kpc^2) at a galactic radius of $r_{gal} \sim 1.24 R_{25}$ with R_{25} 6.44 ($= D_{25}/2$) from the optical center at (R.A., decl.)$_{J2000}$ = (13:37:00.4, −29:52:04.1) (de Vaucouleurs et al. 1991). We revisit a smaller area of $\sim 0\farcm75 \times 0\farcm85$ within the CO(2−1) field at a mass sensitivity that is higher by a factor of about 10 in the CO(3−2) line emission, as well as in the Band 7 dust continuum emission.

M83 presents a prototype XUV disk (Thilker et al. 2005). Deep Hα imaging with the Subaru telescope revealed H II regions over the XUV disk, including some in the region of this study (Koda et al. 2012b). The metallicity is about constant across the XUV disk and is as low as 12 + log(O/H) ∼ 8.2 ("preferred abundances" by Bresolin et al. 2009, from their analyses with multiple metallicity indicators).[12] This is ∼0.4 $Z_\odot$ by adopting the solar abundance of 12 + log(O/H)$_\odot$ = 8.66 (Asplund et al. 2005), which is similar to that of the LMC (∼0.3–0.5 $Z_\odot$, Westerlund 1997). With Spitzer infrared images, Dong et al. (2008) concluded that the SF has been ongoing for at least 1 Gyr. The SF efficiency derived with atomic hydrogen (H I) data indicates a gas consumption timescale much longer than the Hubble time (Bigiel et al. 2010). This extremely low SF efficiency could be due to physical processes either on large scales (e.g., low H I-to-H_2 phase transition) or on small scales (e.g., low SF rate within molecular clouds). Observations and detection of molecular gas would improve our understanding of SF in this extreme environment.

2. Observations and Data

2.1. ALMA Observations

We observed a region of $\sim 0\farcm75 \times 0\farcm85$ (∼0.98 × 1.11 kpc^2; approximately ∼1 kpc^2) in the outskirts of M83 with ALMA's 12 m array in CO(3−2) and Band 7 dust continuum emission. Figure 1 shows the target region: the left panel displays the global context of the galaxy, and the right panels show the observed region with magenta boxes (smaller boxes). The outer (cyan) contour in the left panel shows the extent of the H I disk, which also encloses the XUV disk and numerous UV blobs (the color image). The red boxes in all panels show the region of the previous CO(2−1) and Band 6 continuum emission data (Bicalho et al. 2019). Our region is selected around the position of maximum H I 21 cm intensity within the CO(2−1) observation. It includes bright UV peaks located at the galactocentric distance of ∼1.24 R_{25} (∼8.′0, ∼10.4 kpc), and is outside the traditional optical disk (green contour).

The CO(3−2) line ($\nu_{CO(3-2)} = 345.79599$ GHz) and continuum emission in Band 7 were observed with ALMA (project # 2017.1.00065.S). It mosaicked the target region with 17 pointing positions around the map center at (R.A., decl.)$_{J2000}$ = (13:37:05.8, −29:59:57.4). One spectral window (SPW) was configured for the line emission with a bandwidth of 1.875 GHz (1626 km s^{-1}) with 1920 channels of 976.6 kHz width (0.8466 km s^{-1}). The other three SPWs were configured to cover different sky frequencies for the continuum emission with a bandwidth of 2 GHz with 128 channels for each SPW. The central frequency of the continuum emission is 349.498 GHz (hereafter, 349 GHz continuum emission). The full mosaic observations were repeated six times, resulting in six execution blocks. The final *uv*-coverage at the CO(3−2) frequency extends over the angular scales of 0.″57–13.″7 (∼12–299 pc).

The CO(2−1) line ($\nu_{CO(2-1)} = 230.53800$ GHz) and continuum emission in Band 6 were taken in project # 2013.1.00861.S and were re-reduced for consistency within this study. These data have been studied by Bicalho et al. (2019), and the details of the observations are found there. The rectangular $1\farcm5 \times 3'$ region includes the area of the CO(3−2) and Band 7 continuum data. The bandwidth and channel width are 1.875 GHz (2438 km s^{-1}) and 1.953 MHz (2.540 km s^{-1}) for the CO(2−1) emission. The central frequency for the continuum emission is 224.516 GHz (hereafter, 225 GHz continuum emission). The angular scales covered are 0.″49–10.″7 (∼11–233 pc) at the CO(2−1) frequency.

These data are calibrated using the data reduction scripts provided by the ALMA observatory using the Common Astronomy Software Application (CASA: McMullin et al. 2007). The amplitude and phase of bandpass and gain calibrators are confirmed to be flat over time and frequency after the calibrations.

For the CO(3−2) and CO(2−1) lines we generate data cubes with the TCLEAN task in a standard way. We use a cell size of 0.″15 and channel width of 2.54 km s^{-1} (i.e., the channel width of the CO(2−1) data) over a velocity range of ∼400–700 km s^{-1}. While we use the 2.54 km s^{-1} cube throughout this study unless otherwise specified, we also make a separate CO(3−2) data cube with a channel width of 1.00 km s^{-1}. This cube is used solely for a measurement of velocity dispersions of molecular clouds. The 349 and 225 GHz continuum data are imaged with the multifrequency synthesis mode of TCLEAN. The CO(2−1) and 225 GHz continuum data are regridded to the image format of the CO(3−2) and 349 GHz continuum data for comparisons. The parameters of the data are listed in Table 1, including the total

[12] The scatters in measured metallicities are large among adopted metallicity indicators and among individual H II regions. Within our ALMA coverage, Bresolin et al. (2009) could apply the direct method, the most reliable indicator, to only one H II region (#39 in their catalog) and obtain 12 + log(O/H) ∼ 8.05 ± 0.07 (∼0.3 $Z_\odot$). Bresolin et al. (2009) also obtained 8.24, 8.19, and 8.45 with the [N II]/[O II] indicator, and 8.34, 8.37, and 8.43 with the N2 indicator for H II regions #39, 40, and 41, respectively. They analyzed much larger areas than our ALMA coverage, and from totality they suggested a constant metallicity of 12 + log(O/H) ∼ 8.2 for the full XUV disk.

bandwidth for continuum, the channel width for lines, the cell/pixel size, beam size (its major and minor axis diameters, $b_{\rm maj}$, $b_{\rm min}$, and position angle PA), and rms noise.

2.2. Supplementary Data

We obtained the H I 21 cm data with the Green Bank Telescope (GBT; project 20A–432) and combined them with the archival Karl G. Jansky Very Large Array (VLA) data (projects 13B-194 and 14B-192). We reduced the data in the standard way with GBTIDL and CASA, respectively. The GBT and VLA data are combined after imaging with CASA's feather task. The beam size of the GBT+VLA data is 15″. The details of the observations and data reduction will be presented in a separate publication.

The Hα narrowband image was obtained from narrowband (NA656) and broadband (*Rc*) photometry with the Subaru Prime Focus Camera (Suprime-Cam) on the Subaru telescope. The seeing was about 1″. The observations and data reduction were similar to those presented in Koda et al. (2012b), who used the privately owned old Hα filter (NA659). M83 was reobserved with the observatory-owned filter in the context of a separate, larger Hα survey of galaxies for consistency. The photometric zero-points were calibrated using the Pan-STARRS1 Surveys (PS1) Data Release 1 catalog (Chambers et al. 2016). We followed the procedure described in Yagi et al. (2013) and converted from the PS1 to the Suprime-Cam photometric system using stellar photometry. The flux errors are about 10% or less, and the old and new measurements are consistent within the errors. Note that discussions in this paper require a flux accuracy of only a factor of ∼2. The details of the Hα data will be presented in a separate paper.

3. Auxiliary Information

3.1. H II Regions

A classification of H II regions is not within the scope of this paper, but for the purpose of rough evaluation of SF activity in the observed region, we visually identified significant Hα peaks in the Subaru Hα image. Table 2 lists the ID, coordinates, aperture radius $r_{\rm ap}$, and Hα luminosity $L_{\rm HB}$. Figures 1(e) and (f) show their locations. $L_{\rm HB}$ ranges from 1×10^{35} to 3×10^{37} erg s^{-1}.[13] We do not apply an extinction correction since it is expected to be small (Gil de Paz et al. 2007b) and is negligible for the discussion here, which requires only order-of-magnitude estimations. Our H II regions (B, F, J) correspond to (#09, #08, #07) in Gil de Paz et al. (2007b) and (#39, #41, #40) in Bresolin et al. (2009). The total Hα luminosity in our 1 kpc^2 region is $\sim 6.8 \times 10^{37}$ erg s^{-1}. The identified H II regions contain about 80% of the total luminosity.

As a reference, a model calculation by Sternberg et al. (2003) suggests that a single B0-type star can produce an H II region of $L_{\rm HB}$ 1.4 10^{36} erg s ^{1} assuming Case B recombination and an electron temperature of 10^4 K. The H II regions brighter than this likely have O-type stars, but they have to be relatively late O-type, as an H II region around a single O6-type star can already be as bright as 2.7×10^{37} erg s^{-1}, similar to the brightest in our XUV region. As we see below, the observed XUV region has SF activity similar to, or slightly less than, that of the Orion Nebula, a relatively minor OB star-forming region in the Milky Way (MW).

Table 2
Visually Identified H II Regions

ID	R.A. (J2000)	Decl. (J2000)	$r_{\rm ap}$ (arcsec)	$L_{\rm HB}$ (erg s^{-1})
A	13:37:05.23	−29:59:33.2	2.0	5×10^{36}
B	13:37:04.98	−29:59:45.9	3.1	3×10^{37}
C	13:37:06.41	−29:59:49.3	2.8	2×10^{36}
D	13:37:05.13	−29:59:50.4	1.4	3×10^{35}
E	13:37:05.31	−29:59:50.6	1.1	1×10^{35}
F	13:37:06.60	−29:59:56.4	4.7	1×10^{37}
G	13:37:05.06	−29:59:58.5	2.7	9×10^{35}
H	13:37:05.94	−30:00:02.9	1.9	1×10^{36}
I	13:37:06.27	−30:00:04.5	2.2	1×10^{36}
J	13:37:05.81	−30:00:11.3	2.1	5×10^{36}
K	13:37:05.14	−30:00:14.5	2.4	3×10^{36}

Note. $L_{\rm HB}$ is the Hα luminosity within an aperture of radius $r_{\rm ap}$, which is set by visual judgment (see Figure 1(e)).

3.2. The Orion A Molecular Cloud in the MW

The measured $L_{\rm H_B}$ are similar to those of the Galactic H II regions, M42 and M43. Both of them are in the Orion Nebula, which is located in the OMC-1 dense gas clump in the Orion A molecular cloud.[14] They show $L_{\rm HB}$ 7.1 10^{36} and 3.5×10^{35} erg s^{-1}, respectively (Scoville et al. 2001, from radio continuum observations by Schraml & Mezger 1969). M42 is ionized predominantly by a couple of late O-type stars (O7 and O9) with small contributions from a few B-type stars (Hillenbrand 1997), and M43 is excited by a single B0.5-type star (Simón-Díaz et al. 2011). Hence, individual H II regions in the XUV disk have similar SF activity to that of the Orion Nebula. There are also numerous low-mass stars forming across the Orion A cloud (Großschedl et al. 2019), while their counterparts are not easily detected at the distance of M83.

The Orion A molecular cloud is one of the nearest clouds with massive SF and arguably the most studied high-mass star-forming region. Its internal structure, i.e., a dense gas clump surrounded by a large volume of bulk molecular gas, is common among Galactic molecular clouds; not only among high-mass star-forming clouds (e.g., W49 and W51; Nakamura et al. 1984; Watanabe et al. 2017; Barnes et al. 2020), but also among low-mass star-forming clouds (e.g., Perseus, Serpens, and Ophiuchus; Enoch et al. 2008). Therefore, we use Orion A as our reference cloud. If the Orion A cloud (and Orion Nebula) were in the XUV disk of M83, it would appear as one of brightest UV and Hα blobs. As a gauge of the activity, compared to other Galactic OB associations, Orion A is "not particularly impressive as a massive star-forming region" (Hillenbrand 1997).

The most recent estimation of bulk molecular gas mass in Orion A is $M_{\rm cloud} = 4.0 \times 10^4\ M_\odot$, and its dense clump, OMC-1, has a mass of $M_{\rm clump} = 7.4 \times 10^3\ M_\odot$ (Nakamura et al. 2019).

[13] $L_{\rm HB}$ is from the difference between the narrowband and broadband photometry. Two corrections are accounted for: other line emission in the narrow band assuming [N II]/Hα = 0.2, [S II]/Hα = 0.12, and [O I]/Hα = 0.03 from the measurements by Gil de Paz et al. (2007b) and Hα emission in the broad band (Yagi et al. 2017). It turns out that the overall impact of the two corrections is only about 9% reduction in $L_{\rm HB}$.

[14] We use the nomenclature for Galactic molecular clouds to characterize their nested internal structures. Clumps are dense gas concentrations ($\gtrsim 10^3$ cm^{-3}) within clouds ($\gtrsim 10^2$ cm^{-3}). See Bergin & Tafalla (2007) for details.

Thus, the OMC-1 clump contains about 20% of the cloud mass. We adopt these masses for our discussion, but note that an often-quoted older value of $M_{\rm cloud}$ is about two times larger and is $M_{\rm cloud} = 1.0 \times 10^5\,M_\odot$ after correction for the distance of 414 pc (Dame et al. 1987).

The star formation rate (SFR) within Orion A is estimated with several tracer emissions by Pabst et al. (2021, their Table 5). For comparisons to the XUV disk later, the most relevant is SFR $\sim 7.7 \times 10^{-5}\,M_\odot\,{\rm yr}^{-1}$, based on H$\alpha$ and 24 μm emission. The timescale for gas consumption by the SF is $M_{\rm cloud}/{\rm SFR} \sim 520$ Myr. A caveat is that the SFR estimation in a single cloud is quite uncertain; with the tracers closely related to high-mass SF (Hα, 24 μm, far and total infrared emissions), Pabst et al. (2021) found a range of SFR $= 1.6 \times 10^{-5}$ to $1.0 \times 10^{-4}\,M_\odot\,{\rm yr}^{-1}$. Keeping this uncertainty in mind, we will compare SFR in the XUV disk from Hα on an assumption of negligible extinction, and that in Orion A from Hα and 24 μm by taking extinction into account. Both of these trace the number of UV photons from recently formed massive stars.

4. Results

Figure 2 shows (a) the CO(3−2) integrated intensity map, (b) the CO(3−2) peak intensity map (i.e., maximum value along velocity channels at each spatial pixel), and (c) the Band 7 (349 GHz) continuum map. Only the channels with $>3\sigma$ emission are included for the calculation of (a). Figure 3 shows channel maps. These maps visually display significant detections of the CO(3−2) emission. The continuum map shows no significant emission except for two potential 3.9σ detections at (R.A., decl.) = (13:37:06.7, −30:00:01.9) and (13:37:05.4, −30:00:08.4), which do not coincide with the CO(3−2) emission. Therefore, we discuss mainly the CO(3−2) emission.

4.1. Cloud Identification and Parameters

We identify 23 clouds in the CO(3−2) data in the following way and list them in Table 3. In the data cube, we first identify pixels with $>5\sigma$ peaks and find their envelopes by expanding their volumes to adjacent pixels down to 3σ significance. In some cases the edges of the 3σ envelopes of two peaks (two clouds) are connected. We use the CLUMPFIND algorithm (Williams et al. 1994) to split them—the partition of the two clouds is determined simply by assigning each pixel to the nearest of the two peaks.

We visually inspect the results and manually merge them back to a single cloud when the intensity-weighted positions of the split clouds are closer than the beam size (0.″96) and one velocity pixel (2.54 km s^{-1}). Clouds 4, 8, and 20 are merged back. Cloud 4 might consist of two clouds based on visual inspection, but we strictly apply the same merge criteria for all cases. Figure 2(d) shows the locations of the identified clouds with 2″ diameter circles (about double the beam size). Figure 4 shows the integrated intensity and peak intensity maps of individual clouds. Figure 5 shows the spectra of the clouds. The previous CO(2−1) study did not detect these clouds (Bicalho et al. 2019). In fact, none of them show $>3\sigma$ emission in the CO(2−1) cube (see Section 5.3.1).

Table 3 lists the cloud properties. The first three columns are their intensity-weighted coordinates in R.A., decl., and recession velocity V. FWHMx and FWHMy are the FWHMs in the R.A. ($=x$) and decl. ($=y$) directions and are calculated from intensity-weighted dispersions σ_X (where $X = x$, y). The σ_X are calculated without any model profile, but we convert them to FWHM by assuming a Gaussian distribution (i.e., FWHM $\sqrt{8\ln 2}\,\sigma_X$), so that they can be directly compared to the beam size in FWHM. We note that the major axis of the beam is roughly in the R.A. (x) direction, and the minor axis is in the decl. (y) direction. N_{xy} is the number of spatial pixels with $>3\sigma$ emission in the sky projection. The beam area amounts to $N_{xy} = 40$ in FWHM. $\sigma_{\rm v}$ is the intensity-weighted velocity dispersion calculated with the 1 km s^{-1} cube. Only the pixels with $>3\sigma$ emission in the 1 km s^{-1} cube (red in Figure 5) are included for this calculation. When the number of $>3\sigma$ pixels is less than four, we place only an upper limit in $\sigma_{\rm v}$, assuming the upper limit of the FWHM to be 4 km s^{-1} (i.e., $\sigma_{\rm v} = 1.7$ km s^{-1}). We do not apply deconvolution for the 1 km s^{-1} channel width since it is negligible (i.e., the second moment of the 1 km s^{-1} boxcar comes to only $1/\sqrt{12}$ 0.29 km s^{-1}, and its quadratic subtraction from $\sigma_{\rm v}$ makes only a negligible difference). The peak intensity, $S^{\rm peak}_{\rm CO(3\ 2)}$, and total flux, $S_{\rm CO(3-2)}dv$, are also listed in the table. The error in total flux is calculated by shifting the cloud volume within the 3D data cube in random directions 300 times and by calculating the standard deviation among the shifted volumes.

4.2. Sizes

Some clouds apparently show internal structures in Figure 4 and are on the verge of being spatially resolved. On the other hand, most have FWHM sizes similar to, or smaller than, the beam size. Thus, all clouds, excepts Cloud 4 and 8, are spatially unresolved or only very marginally resolved at the resolution of 0.″96 (21 pc). Clouds 3, 5, and 22 show FWHMx and/or FWHMy larger than the beam size (Table 3), but they suffer from low-level emission (Figure 4). For example, Cloud 3 has a large peculiar extension at around 3σ–4σ significance, which increases FWHMx and FWHMy, but appears spurious. The extended components of Clouds 5 and 22 are also at low level (3σ–4σ). We also note that FWHMy is measured in about the direction of the beam minor axis. It is often smaller than the minor axis size of 0.″82, again because the measurements suffer from the low-level emission.

Clouds 4 and 8 show two peaks in Figure 4, which are merged into a single cloud in our cloud identification process since they are closer than the resolution. We consider them as slightly resolved single clouds with a caveat that they could be a blend of two unresolved clouds.

Even in the marginally resolved cases, measuring cloud sizes is difficult. The cloud radius R may be estimated with the equation $R = 1.92\sigma_{\rm r}$ (Solomon et al. 1987) using the beam-deconvolved average standard deviation in radius,

$$_{\rm r} \quad \sqrt{\frac{\rm FWHM}{8\ln 2}\frac{x}{y}\quad b_{\rm maj}b_{\rm min}}. \qquad (1)$$

Since the measured size is sometimes smaller than the beam size (Table 3), we consider $\sigma_{\rm r}$ and R measurable only when the measured size is at least 20% larger than the beam size (assuming that FWHMx and FWHMy are measured with 20% accuracy). This sets the minimum measurable R to be R $0.54\sqrt{b_{\rm maj}b_{\rm min}}$ 0.48 (10.5 pc). Otherwise, we have only an upper limit of 10.5 pc. In this way, only one cloud with the spurious extension (Cloud 3; Figure 4) gives a

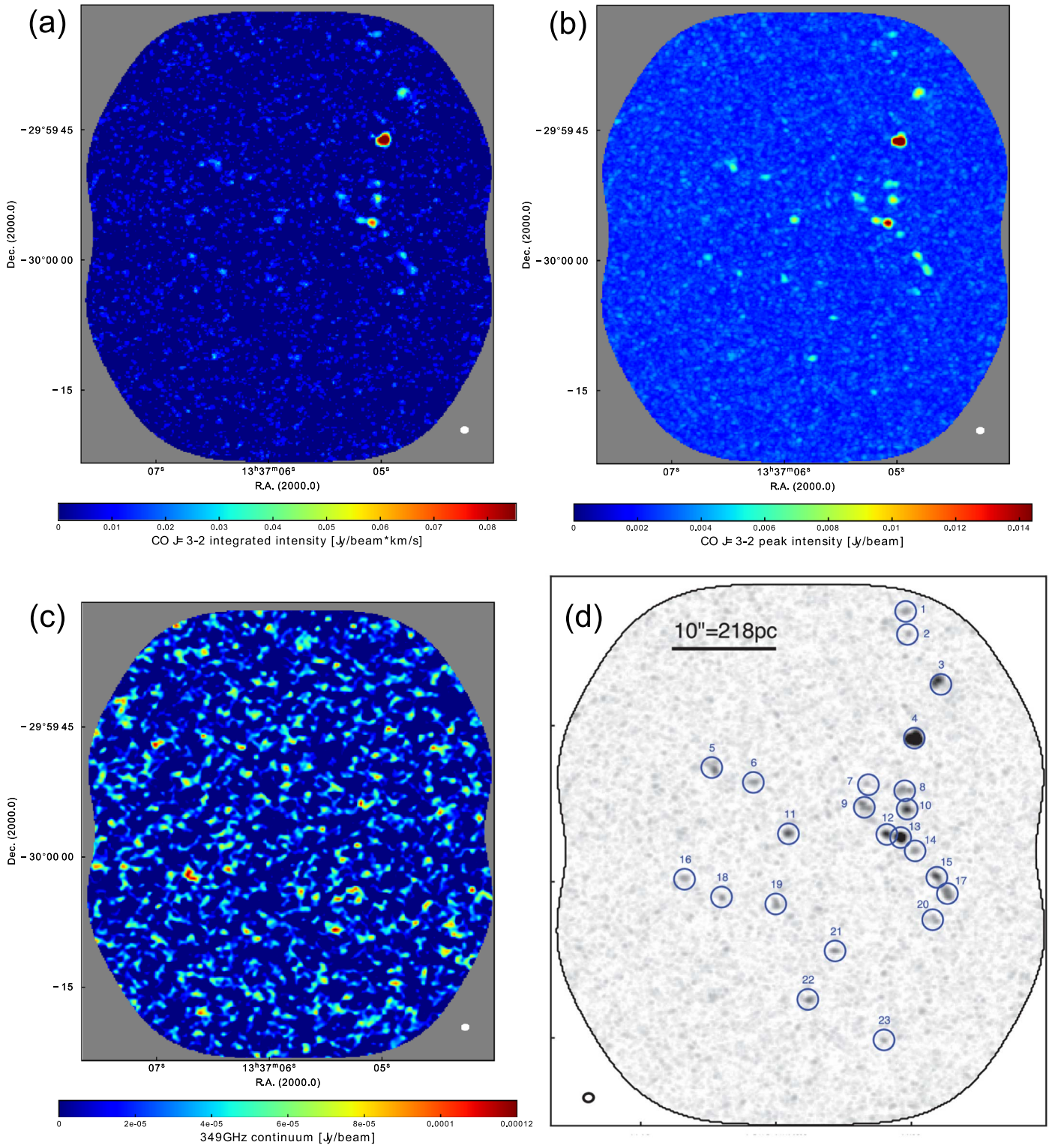

Figure 2. (a) CO(3−2) integrated intensity map. (b) CO(3−2) peak intensity map. (c) Band 7 (349 GHz) continuum map. (d) Molecular clouds on the CO(3−2) peak intensity map. Cloud IDs are indicated and correspond to the ones in Table 3. Each circle has a diameter of 2″. The beam size of $0\farcs96 \times 0\farcs82$ (PA $= -84\fdg7$) is shown in the bottom left corner, corresponding to 21×18 pc^2 at 4.5 Mpc.

measurable R, while, as discussed, it suffers from the error. Therefore, the CO(3−2)-emitting parts in the detected clouds (their diameters) are smaller than the resolution of 21 pc.

As a reference, the Orion A cloud has a whole extent of ∼20 pc when it is observed in the CO(1–0) or CO(2−1) emission, which trace the bulk molecular gas (Sakamoto et al. 1994; Kong et al. 2018; Nakamura et al. 2019). Its star-forming dense clump OMC-1 occupies only a small area (∼2 pc) at the heart of the cloud and is bright in CO(3−2) (Ikeda et al. 1999). It is possible that our detected CO(3−2) peaks are mainly from dense clumps within molecular clouds, and hence are unresolved.

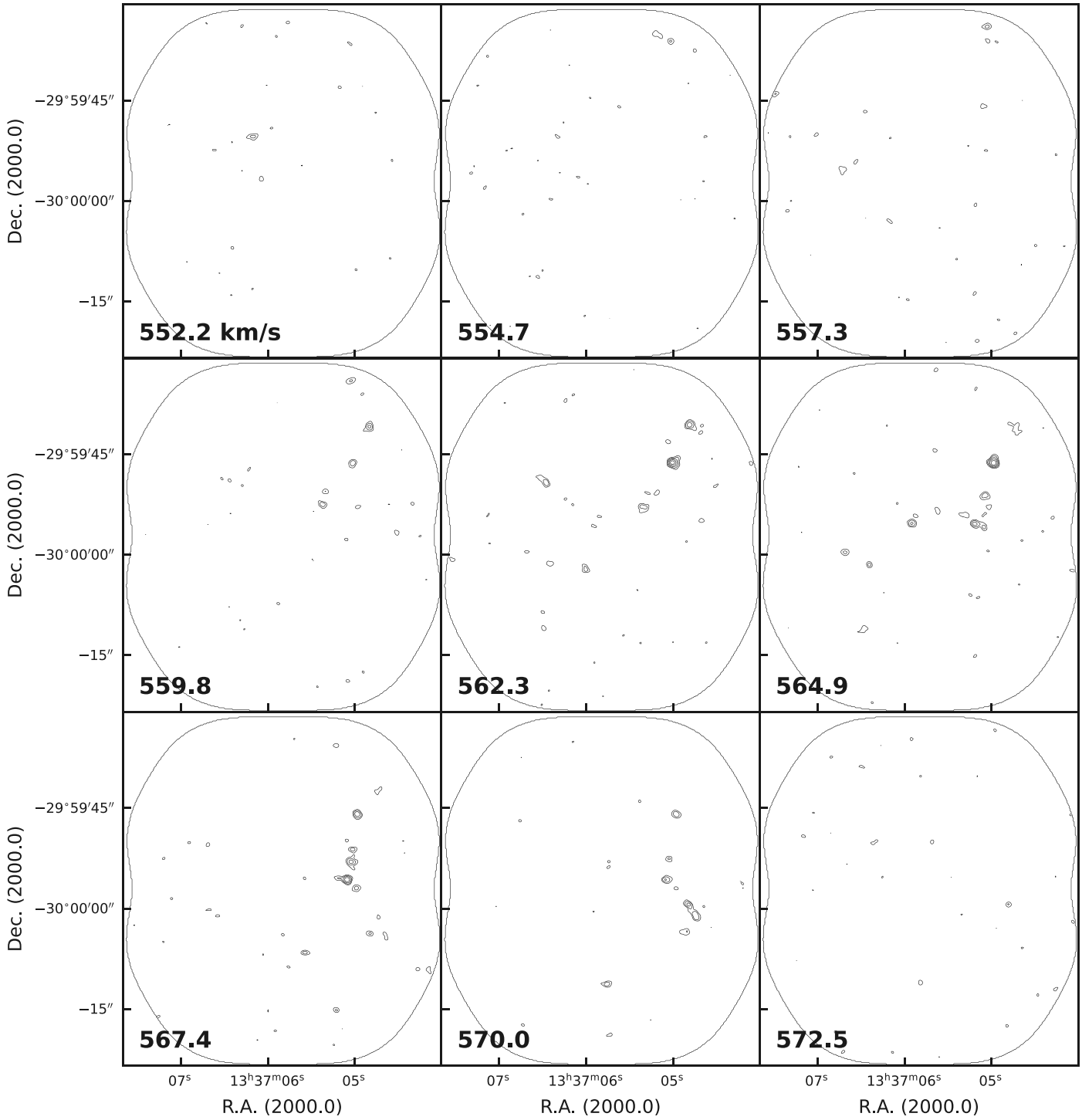

Figure 3. CO(3−2) channel maps with the field of view of the ALMA observations outlined. Channel velocities are shown in the bottom left corner. The rms noise is 0.96 mJy beam^{-1} in the 2.54 km s^{-1} channel, and the contours are at 3σ, 5σ, 8σ, 12σ, and 17σ significance.

4.3. Velocity Widths

The velocity widths of most clouds are resolved in the 1 km s^{-1} cube (see σ_v in Table 3). Cloud 3 has a relatively large σ_v due to the spurious extension. Cloud 4 has a wide width of $\sigma_v = 6.1$ km s^{-1} with a caveat that it could be a blend of two clouds.

Again using Orion A as a reference, the velocity width of the bulk gas, measured in CO(1–0) and averaged over the whole cloud, is about 5 km s^{-1} at 50% of the peak brightness (from Figure 5 of Nakamura et al. 2019). The full CO(3−2) velocity width over the OMC-1 clump (size of about 2 pc) is not found in the literature; toward Orion KL (the brightest region), it is about 7 km s^{-1} at 50% of the peak brightness in a 134″ (∼0.3 pc) beam (from Figure 15 of Masui et al. 2021). Hence, the dense part has a broader linewidth than the entire cloud. These are similar to the velocity widths of Cloud 4 measured in CO(3−2).

Figure 6 plots σ_v against the radius R (mostly the upper limits; see Section 4.2). It also shows clouds in some other

Table 3
Cloud Parameters

(1) ID	(2) R.A. (J2000)	(3) Decl. (J2000)	(4) V (km s^{-1})	(5) FWHMx (arcsec)	(6) FWHMy (arcsec)	(7) N_{xy}	(8) σ_v (km s^{-1})	(9) $S^{peak}_{CO(3\ 2)}$ (mJy beam^{-1})	(10) $S_{CO(3-2)}dv$ (mJy km s^{-1})	(11) M_{clump} ($M_\odot$)	(12) M_{cloud} ($M_\odot$)
1	13:37:05.05	−29:59:34.0	558.5	0.81	0.52	52	2.9	5.59	22.6 ± 2.8	8.1×10^2	2.5×10^3
2	13:37:05.04	−29:59:36.2	555.0	0.59	0.57	39	2.1	5.30	12.6 ± 1.7	4.6×10^2	1.4×10^3
3	13:37:04.79	−29:59:41.0	562.5	1.67	1.46	197	4.6	9.83	79.2 ± 4.9	2.9×10^3	8.7×10^3
4	13:37:04.99	−29:59:46.1	564.4	1.02	0.95	156	6.1	21.68	207.7 ± 7.3	7.5×10^3	2.3×10^4
5	13:37:06.48	−29:59:49.0	562.1	1.13	0.98	85	1.5	7.08	25.5 ± 2.6	9.2×10^2	2.8×10^3
6	13:37:06.17	−29:59:50.4	552.2	0.93	0.50	51	<1.7	5.77	13.4 ± 2.0	4.8×10^2	1.5×10^3
7	13:37:05.32	−29:59:50.6	560.5	0.78	0.48	33	<1.7	4.94	8.1 ± 1.4	2.9×10^2	8.9×10^2
8	13:37:05.06	−29:59:51.2	565.8	1.13	0.60	83	3.6	6.21	28.3 ± 3.0	1.0×10^3	3.1×10^3
9	13:37:05.35	−29:59:52.8	561.4	0.93	0.89	96	2.9	7.06	33.8 ± 3.3	1.2×10^3	3.7×10^3
10	13:37:05.04	−29:59:53.0	567.5	0.82	0.95	101	3.3	9.55	43.4 ± 3.5	1.6×10^3	4.8×10^3
11	13:37:05.91	−29:59:55.3	564.6	0.73	0.70	62	<1.7	8.39	22.2 ± 2.3	8.0×10^2	2.4×10^3
12	13:37:05.19	−29:59:55.4	565.5	0.77	0.60	61	2.4	9.73	30.7 ± 2.9	1.1×10^3	3.4×10^3
13	13:37:05.09	−29:59:55.7	567.7	0.84	0.71	89	3.4	15.70	74.0 ± 4.2	2.7×10^3	8.1×10^3
14	13:37:04.98	−29:59:57.0	567.8	0.70	0.52	45	<1.7	5.96	14.5 ± 1.9	5.2×10^2	1.6×10^3
15	13:37:04.82	−29:59:59.5	570.4	0.76	0.87	75	2.4	9.01	29.2 ± 2.6	1.1×10^3	3.2×10^3
16	13:37:06.68	−29:59:59.7	564.9	0.65	0.67	51	3.5	5.33	15.0 ± 2.2	5.4×10^2	1.6×10^3
17	13:37:04.75	−30:00:01.1	569.8	0.77	0.91	78	1.7	7.21	27.3 ± 2.7	9.8×10^2	3.0×10^3
18	13:37:06.41	−30:00:01.4	563.8	0.57	0.53	38	<1.7	6.02	14.1 ± 1.9	5.1×10^2	1.5×10^3
19	13:37:06.01	−30:00:02.1	562.3	0.61	0.75	46	<1.7	5.81	12.7 ± 1.7	4.6×10^2	1.4×10^3
20	13:37:04.85	−30:00:03.6	569.0	0.96	0.55	61	2.2	5.43	19.2 ± 2.3	6.9×10^2	2.1×10^3
21	13:37:05.57	−30:00:06.6	567.4	0.72	0.41	34	<1.7	6.30	9.4 ± 1.4	3.4×10^2	1.0×10^3
22	13:37:05.77	−30:00:11.2	570.5	1.02	0.53	58	1.6	6.78	16.9 ± 1.9	6.1×10^2	1.9×10^3
23	13:37:05.21	−30:00:15.1	566.9	0.57	0.40	26	1.7	5.23	7.4 ± 1.3	2.7×10^2	8.2×10^2

Note. (1) Cloud ID. (2), (3) Coordinates. (4) Recession velocity V. (5), (6) FWHMs in R.A. ($=x$) and decl. ($=y$) directions, calculated from intensity-weighted dispersions and assuming a Gaussian profile. (7) Number of pixels with $>3\sigma$ emission in the sky projection. (8) Velocity dispersion measured with the 1 km s^{-1} cube. (9) Peak intensity within the cloud. (10) Total flux of the cloud. The error is a random error and does not include systematic errors. (11), (12) Clump and cloud masses, including CO-dark H_2 as well as He. $M_{cloud} = M_{clump}/0.34$. Note that the beam-deconvolved radius R is not listed, since it is only an upper limit ($R < 0\farcs48$) for all clouds except Cloud 3 ($R = 1\farcs05$), whose measurement suffers from the spurious extension (see Section 4.2).

galaxies (Solomon et al. 1987; Bolatto et al. 2008; Wong et al. 2011; Rubio et al. 2015), with notes that they are measured in CO(1−0) or CO(2−1) while our XUV clouds are in CO(3−2) and that the different CO transitions may trace different parts of clouds (Section 5). For their measured σ_v, our XUV clouds generally have smaller (or similar) sizes compared to the clouds in the other galaxies. This makes sense if the CO(3−2) emission is primarily tracing dense clumps within the clouds, as seen in Orion A.

4.4. Distribution

The 23 clouds are distributed over a large area across the 1 kpc^2 field of view (Figures 2(d) and 3). Their overall distribution shows some coherent (not random) structures, which appear like chains of clouds. These chains extend over 600 pc in length, or potentially longer beyond the field of view. The cloud distribution also shows a large-scale velocity gradient in the channel maps (Figure 3). From the low to high velocity channels, it spatially shifts from the northeast to the southwest side.

Figure 7 shows the cloud locations on the Hα, UV, and H I images. Clouds 4, 7, 22, 23, and possibly 5, 16, 19, are directly associated with H II regions B, E, J, K, C, F, and H, respectively. Among these, B, J, K, and C are four of the most prominent H II regions in the field. Cloud 4 is the brightest in CO(3−2), while, interestingly, the other three clouds are in the bottom 2/3 of the clouds in total CO(3−2) flux. All the other clouds are in the proximity of, but outside, the H II regions. The variations could be due to an evolutionary sequence of molecular clouds or to the stochasticity of massive SF in this low SF environment (i.e., when the total stellar mass produced in a region is low, clouds may not always produce stars over the full mass spectrum. The stellar initial mass function may be filled stochastically, but not completely; Koda et al. 2012b). With respect to the atomic gas distribution, most clouds and H II regions are around, but not on, the peak of the H I emission.

5. Discussion

5.1. Molecular Clouds in a Low-metallicity Environment

We are using the Orion A molecular cloud as a fiducial reference cloud given the similarity of its SF activity to the (brightest) clouds in the XUV disk. Orion A has an internal mass distribution common among other large and small Galactic molecular clouds, having small star-forming dense clump(s) embedded deeply in thick layers of bulk molecular gas (Nakamura et al. 1984; Enoch et al. 2008; Watanabe et al. 2017; Barnes et al. 2020). Figure 8(a) schematically illustrates this mass distribution. In terms of CO emissions, CO(1−0) and CO(2−1) can be excited easily at an average density and temperature in molecular clouds ($\sim 10^2$ cm^{-3}, $\sim$10 K; Scoville & Sanders 1987), and hence the bulk gas contributes significantly to their total CO(1−0) and CO(2−1) luminosities (Kong et al. 2018; Nakamura et al. 2019). By having the $J = 3$ level temperature of $E_{J=3}/k \sim 33.2$ K and critical density of $>10^3$ cm^{-3}, the CO(3−2) emission requires higher density and temperature than the averages for excitation and is radiated predominantly from the dense clumps (Ikeda et al. 1999). Once

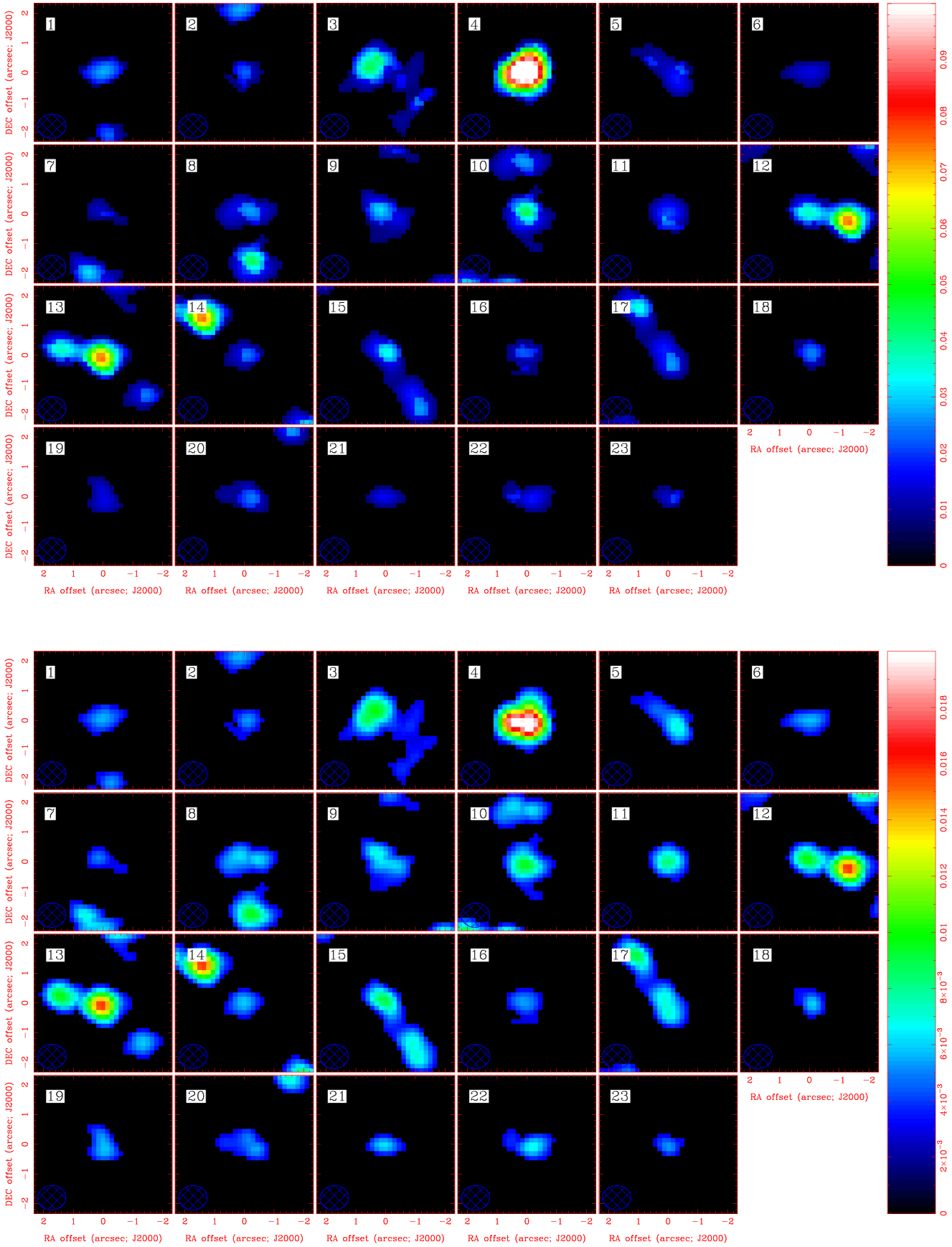

Figure 4. Postage stamp images of individual clouds. Only the pixels with $>3\sigma$ emission in the data cube are used for these images. The peaks at the center of each image are the clouds of interest. Surrounding clouds, when they exist, are also in the images. Top: integrated intensity maps in units of Jy beam^{-1} km s^{-1}. Bottom: peak intensity maps in units of Jy beam^{-1}. The hatched ellipses in the bottom left corners indicate the beam size.

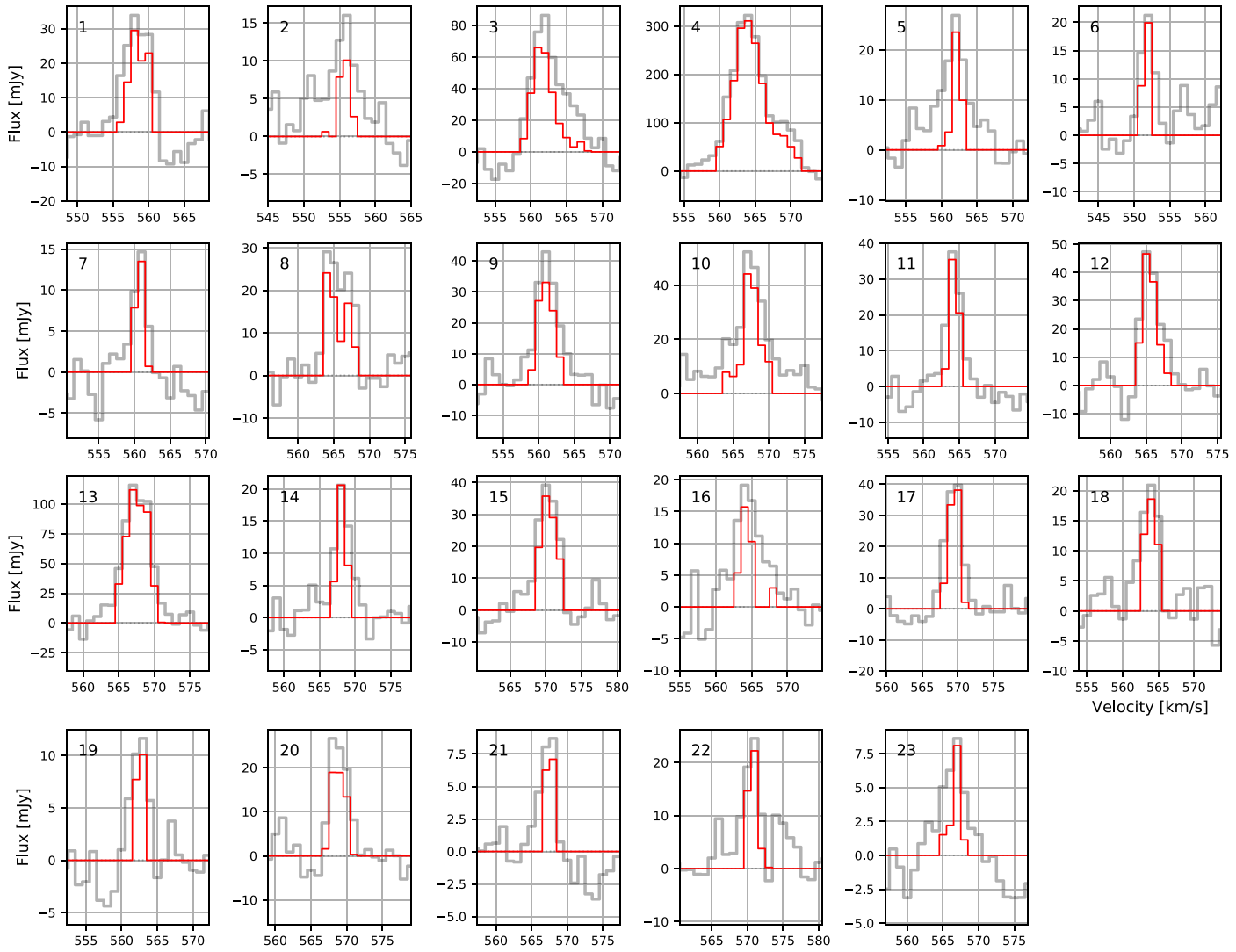

Figure 5. CO(3−2) spectra of the clouds produced with the 1 km s^{-1} cube. The spatial pixels and volume that each cloud occupies in the (R.A., decl., velocity) space are determined with the 2.54 km s^{-1} cube. The gray spectra show the sum over all the spatial pixels including noises in each 1 km s^{-1} channel. The red spectra include only the pixels with $>3\sigma$ emission in the cloud volume.

it is excited in thermalized gas, CO(3−2) can become brighter than CO(1−0) and CO(2−1) in total flux.

We hypothesize that the clouds in the XUV disk share the common clump–envelope mass distribution of the Galactic molecular clouds. The common mass structure is expected for gravitationally bound clouds because it is determined predominantly by the internal physics rather than the environment.

Even when the mass distribution is the same, the chemical structure and appearance of the clouds in the CO emissions depend on the metal abundance (e.g., Maloney & Black 1988; van Dishoeck & Black 1988; Israel 1997; Pak et al. 1998; Wolfire et al. 2010). In high metallicity ($\sim$1 $Z_\odot$; Figure 8(a)), the bulk gas in clouds can be detected in the low excitation transitions ($J = 1$–0 or 2–1) of CO—the brightest and second-most-abundant molecule after H_2. In low metallicity (<1 $Z_\odot$; Figure 8(b)), the dust extinction is low, and the ambient stellar radiation can penetrate deeper into the clouds. This radiation dissociates more CO in their outer layers through CO line absorptions, while the abundant H_2 molecules can be self-shielded. This differential photodissociation makes the cloud's outer layers CO-deficient and CO-dark while still H_2-abundant (Figure 8(b)).

The ambient radiation can come from the UV-emitting sources across the 1 kpc^2 region (Figure 1(f)) and be potentially as strong as that in the solar neighborhood. There are several Orion-class SF regions within the region (Table 2, Figure 7). In the solar neighborhood, the Orion cloud is the closest massive SF region, at a distance of 414 pc.

In addition to this photodissociation model for the cloud envelopes, we hypothesize that the dense clumps reside in the self-shielded, CO-abundant part of the clouds. The clouds in the XUV disk may suffer from this differential photodissociation due to the low metallicity. With this hypothesis, we can consistently explain the detection of CO(3−2), which is mainly from the dense clumps, the nondetection of CO(2−1), and Hα luminosities, tracing SF activity.

5.2. Dense Clumps in the Hearts of Clouds

In our hypothesis, the dense clumps can be shielded from photodissociation and radiate CO emission even in the low-metallicity environment (Figure 8(b)). The fractions of the CO-abundant part and dense clumps over entire clouds can be crudely estimated from a combination of previous measurements

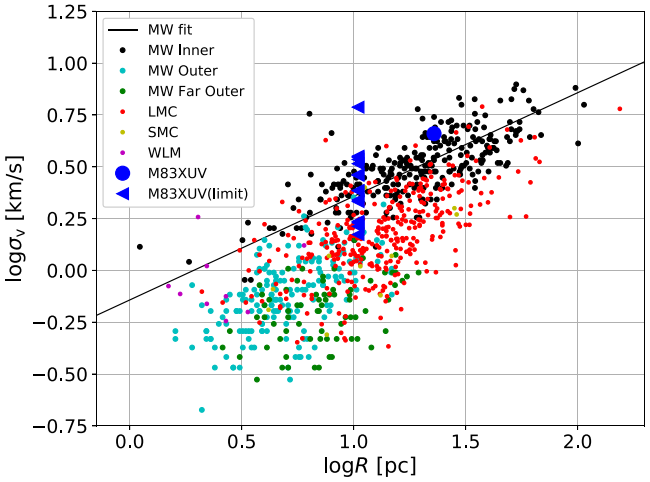

Figure 6. Plot of cloud radius vs. velocity dispersion. M83 XUV clouds are blue (and the blue arrows are the upper limits in radius, while they are resolved in velocity). Reference points in the background are for the MW's inner disk (Solomon et al. 1987), outer disk ($r_{gal} \sim$ 12–14 kpc; Sun et al. 2017), and far outer disk (∼14–22 kpc; Sun et al. 2015), and for the Large and Small Magellanic Clouds (Bolatto et al. 2008; Wong et al. 2011) and the galaxy WLM (Rubio et al. 2015). The solid line is a fit to the inner disk clouds (Solomon et al. 1987).

of the mass-to-light ratio M_{cloud}/L_{CO}—between the cloud's total mass M_{cloud} and CO luminosity L_{CO}. The ratio M_{cloud}/L_{CO} is often denoted as the CO-to-H_2 conversion factor X_{CO} and $X_{CO} \propto M_{cloud}/L_{CO}$.[15] The following estimation supports the hypothesis that the dense clumps are indeed protected even in low metallicity, and thus can radiate CO(3−2) emission as much as their counterparts in high metallicity.

Clouds of the same mass M_{cloud} in high and low metallicity have different amounts and distributions of CO molecules (Figures 8(a) and (b)). Those in low metallicity show a smaller L_{CO}, and hence larger X_{CO}. This difference is detected using the virial mass measurements of molecular clouds with CO(1−0): $X_{CO(1-0)} = 3 \times 10^{20}$ in the Milky Way (∼1 $Z_\odot$; Scoville et al. 2016) and 7×10^{20} in the LMC (∼0.4 $Z_\odot$; Fukui et al. 2008). Therefore, for the same mass M_{cloud}, clouds in the LMC emit only about 40% of $L_{CO(1-0)}$ compared to their Galactic counterparts. In other words, only about 40% of molecular gas, presumably at cloud centers, would have CO molecules at the LMC metallicity.

The 40% of molecular gas that has CO likely hosts dense clumps at the cloud centers (Figure 8(b)). The CO(3−2) emission requires higher density and/or kinetic temperature for excitation than CO(1−0) and CO(2−1), and preferentially traces the dense clumps rather than the bulk gas (e.g., Komugi et al. 2007; Wilson et al. 2009). Wilson et al. (2009) compared the CO(3−2) luminosity $L_{CO(3-2)}$ against the bulk mass M_{cloud} in nearby galaxies at solar metallicity (∼1 $Z_\odot$). Their result suggests that the detected $L_{CO(3-2)}$ values are only 34% of those expected from $L_{CO(1-0)}$ on an assumption of thermalized gas (i.e., the CO 3–2/1–0 ratio in the brightness temperature is about unity). Thus, only about 34% of molecular gas in clouds radiates CO(3−2) emission at the high metallicity (more accurately, the molecular gas that emits about 34% of $L_{CO(1-0)}$ radiates CO(3−2) emission). Therefore, at LMC metallicity, we expect that the dense clumps emitting at CO(3−2) (34% of the molecular gas) are located in the same region as the gas that is protected from photodissociation and has CO molecules (40% of the molecular gas), as in Figure 8(b).

Leroy et al. (2022) recently found a CO 3–2/1–0 ratio of 0.31 (0.20–0.42 at 16th to 84th percentiles) as a galaxy-integrated mean value of 20 massive galaxies of solar metallicity. This is consistent with our adopted ratio of 0.34 from Wilson et al. (2009). Our discussions in this paper are for typical, Orion-class SF regions (Section 3.1), but the ratio may increase mildly in regions of more intense SF (Miura et al. 2012, 2014; Onodera et al. 2012; Vlahakis et al. 2013; Morokuma-Matsui & Muraoka 2017).

5.3. Masses of Molecular Clouds and Clumps

Even when the cloud outer layers become CO-dark in low metallicity, there are still abundant H_2 molecules there, and M_{cloud} does not depend on the metallicity. In our hypothesis, the dense clumps are protected from photodissociation and would radiate a similar amount of $L_{CO(3-2)}$ in high and low metallicities. Hence, the calibration of $M_{cloud}/L_{CO(3-2)}$ in high metallicity should be applicable in low metallicity, and the conversion equation from $L_{CO(3-2)}$ to M_{cloud} derived in high metallicity can be used here. We adopt the calibration by Wilson et al. (2009),

$$M_{cloud} \quad 1.1 \quad 10^5 M \left(\frac{S_{CO(3\ 2)}dv}{1\ \mathrm{Jy\ km\ s^{-1}}}\right)\left(\frac{D}{4.5\ \mathrm{Mpc}}\right)^2 \left(\frac{R_{3\ 2/1\ 0}}{0.34}\right)^{-1}\left(\frac{X_{CO(1\ 0)}}{3.0\quad 10^{20}}\right), \tag{2}$$

where the CO(3−2) flux $S_{CO(3-2)}dv$ is related to the luminosity $L_{CO(3-2)} = 4\pi D^2 S_{CO(3-2)}dv$. $R_{3\ 2/1\ 0}$ is the CO 3–2/1–0 brightness temperature ratio averaged over galaxies with high metallicity. The $X_{CO(1-0)}$ term is from the calibration made in the high metallicity, and hence the $X_{CO(1-0)}$ in high metallicity should be used here even when it is applied in low metallicity. M_{cloud} from CO(3−2) is listed in Table 3 and ranges from $8.2 \times 10^2\ M_\odot$ to $2.3 \times 10^4\ M_\odot$.

The derived masses are much lower than the previous detections in XUV disks (Braine & Herpin 2004; Braine et al. 2007, 2010, 2012; Dessauges-Zavadsky et al. 2014). From their high abundance in our region, the low-mass molecular clouds are likely a more common cloud population in XUV disks than previously detected. The most massive cloud (Cloud 4) has a mass similar to that of Orion A. Its SF activity measured in $L_{H\alpha}$ is also similar to that of the Orion Nebula in Orion A (Section 3.2). Note again that among massive star-forming regions in the MW, Orion A is one of the least impressive. All the other clouds in our study have H II regions in their proximity, but are less massive and less active in SF. The least massive cloud of ∼800 $M_\odot$, only 4% of Orion A's mass, is unlikely to form OB stars. The SF in the XUV disk appears to be limited by the cloud masses.

The CO(3−2) emission is mainly from dense clumps in the clouds since it requires high density and temperature for excitation. We attempt a crude estimation of the clump masses M_{clump} under a set of assumptions: (1) the clumps do not suffer from photodissociation and have CO molecules, (2) X_{CO} can be applied to a part (clump) of a cloud, and (3) the gas is thermalized (the CO 3–2/1–0 brightness temperature ratio within the clump, $R_{3-2/1-0}$, is unity). In this case, we should

[15] In units of $H_2\ \mathrm{cm}^{-2}[\mathrm{K\ km\ s}^{-1}]^{-1}$, which will be omitted in the rest of the main text.

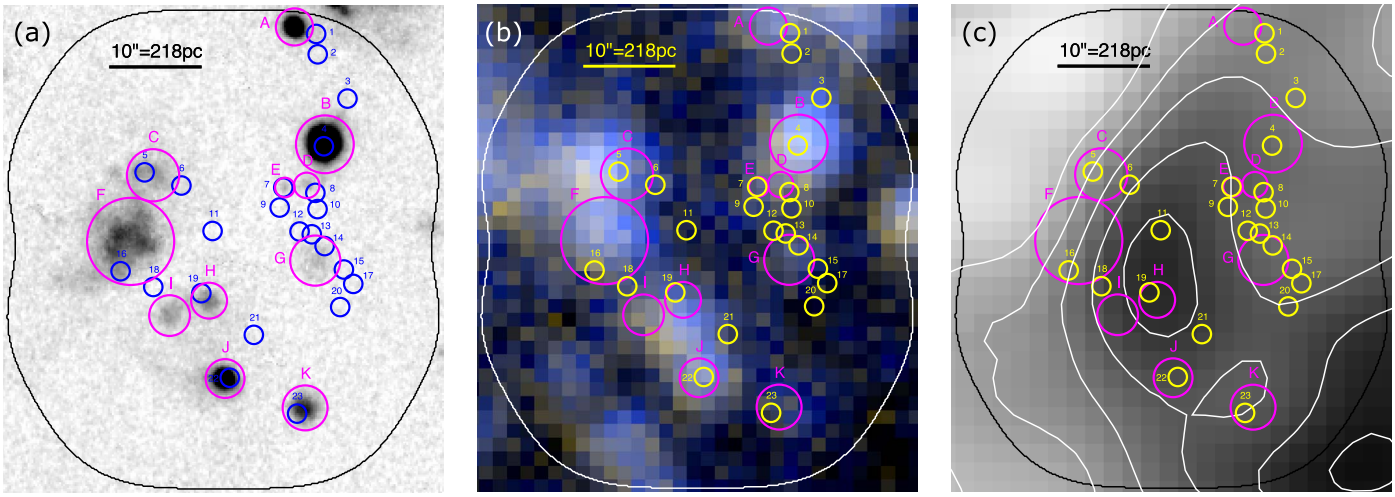

Figure 7. (a) Subaru Hα image at a resolution of about 1″. (b) GALEX FUV and NUV-band color composite image at a resolution of about 5″ (Gil de Paz et al. 2007a). (c) VLA + GBT H I 21 cm image (grayscale) with contours—from the brightest—at 0.30, 0.25, 0.20, 0.15, 0.10, and 0.05 Jy beam^{-1} km s^{-1} with the 15″ beam. The brightest contour corresponds to the H I surface density of ∼12 $M_\odot$ pc^{-2} (and 16 $M_\odot$ pc^{-2} for H I + He). Magenta circles denote the H II regions identified by eye with the labels "A," "B," "C," .... The Hα luminosities $L_{\rm HB}$ enclosed within each circle are listed in Table 2. Blue or yellow circles are molecular clouds and are the same as the ones in Figure 2(d) with the labels "1," "2," "3," ....

adopt $X_{\rm CO} = 3 \times 10^{20}$ from the Galactic measurement even for the low metallicity, because no part of the clump is photodissociated. It gives

$$M_{\rm clump} \quad 3.6 \quad 10^4 M \left(\frac{S_{\rm CO(3\ \ 2)}dv}{1\ {\rm Jy\ \ km\ s^{\ 1}}}\right)\left(\frac{D}{4.5\ {\rm Mpc}}\right)^2 \left(\frac{R_{3\ \ 2/1\ \ 0}}{1.0}\right)^{\ 1}\left(\frac{X_{\rm CO(1\ \ 0)}}{3.0\quad 10^{20}}\right). \tag{3}$$

The 1σ sensitivity in the 2.54 km s^{-1} cube of CO(3−2) is 88 $M_\odot$. $M_{\rm clump}$ ranges from $M_{\rm clump} = 2.7 \times 10^2$ $M_\odot$ to 7.5×10^3 $M_\odot$ (Table 3). Given the assumptions, we expect the total uncertainties to be not smaller than a factor of 2–3. Again, the mass of the clump in Cloud 4 is about the same as that of the OMC-1 clump in the Orion A cloud.

5.3.1. Consistency with CO(2−1) and Dust Measurements

The detections in CO(3−2) are consistent with the previous nondetections in CO(2−1) (Bicalho et al. 2019). The CO(3−2)-emitting clumps should also radiate the CO(2−1) emission as well, but their CO(2−1) intensities are below the detection limit. For example, Cloud 4, the brightest, has a total CO(3−2) flux of $S_{\rm CO(3-2)}dv = 207.7$ mJy km s^{-1} over the velocity width of 12.7 km s^{-1} (five channels). Adopting the Rayleigh–Jeans approximation for thermalized gas, this translates to a total CO(2−1) flux of $S_{\rm CO(2-1)}dv = 92.3$ mJy km s^{-1}. From Table 1, the 1σ sensitivity in CO(2−1) over the same velocity width is 60.2 mJy km s^{-1}. The brightest cloud/clump is only at a 1.5σ significance in the CO(2−1) measurement, explaining the nondetection in CO(2−1).

If Cloud 4, the most massive, were to be filled with CO like clouds in high metallicity (Figure 8(a)), its mass of 2.3×10^4 $M_\odot$ would emit a total CO(2−1) flux of $S_{\rm CO(2-1)}dv = 200$ mJy km s^{-1}, using $X_{\rm CO(1-0)} = 3.0 \times 10^{20}$ in the high-metallicity regime and a CO(2−1) to CO(1−0) brightness ratio of $R_{2-1/1-0} \sim 0.7$ for the bulk gas (Braine & Combes 1992; Hasegawa 1997; Sorai et al. 2001; Koda et al. 2012a, 2020). This should have been detected at 3.3σ in the previous CO(2−1) measurement.

Note that the two assumptions we adopted above—CO being confined only in the clump and being thermalized—*minimize* the predicted CO(2−1) flux for the detected CO(3−2) flux. If the CO(2−1) emission is also from a cloud envelope, it should add to the CO(2−1) flux. If the gas is not thermalized, the CO 3–2/2–1 flux ratio would be lower, and the predicted CO(2−1) flux would be higher. Either way, the CO(2−1) emission from Cloud 4 should have been detected. In other words, it is difficult to deviate significantly from the conditions we assumed.

The CO(2−1) nondetection also excludes the possibility of a CO-bright envelope as large as Orion A's (∼20 pc). The CO(2−1) data can resolve such an envelope at the beam size of $\sim 17 \times 12$ pc^2 at a high sensitivity of 58 mK (1σ) (Table 1). The nondetection suggests that its average surface brightness is <0.17 K (3σ). Hence, the envelope is CO(2−1)-dark.

An independent constraint on $M_{\rm cloud}$ may be derived from the dust continuum emission. Using the calibration by Scoville et al. (2016) in a range of environments and adopting the power-law dependence of the dust emissivity on frequency ν as $\kappa_\nu \propto \nu^\beta$, we obtain

$$M_{\rm cloud} \quad 4.8 \quad 10^8 M \left(\frac{S_{\rm O}}{\rm Jy}\right)\left(\frac{D}{4.5\ {\rm Mpc}}\right)^2\left(\frac{X_{\rm CO(1\ \ 0)}}{3.0\quad 10^{20}}\right) \left(\frac{\rm O}{\rm O_{850\ \ m}}\right)^{\rm (C\ \ 2)}\left(\frac{T_{\rm d}}{25\ {\rm K}}\right)^{\ 1}\left(\frac{\rm o(T_d)}{\rm 850\ m(25\ K)}\right)^{\ 1}, \tag{4}$$

where

$$\rm o(T_d) \quad \frac{x}{e^x \quad 1}, \quad \text{where } x \quad \frac{h\rm O}{k_B T_d}, \tag{5}$$

and $\nu_{850\ \mu{\rm m}} \approx 353$ GHz. The $X_{\rm CO}$ term is due to the calibration in high metallicity. We adopt a dust emissivity index of $\beta = 1.8$ (Planck Collaboration et al. 2011) and dust temperature of $T_{\rm d} = 25$ K (Scoville et al. 2016). The detection limits from the 225 and 349 GHz dust continuum measurements correspond to 1.5×10^6 $M_\odot$ and 4.5×10^4 $M_\odot$ (3σ), respectively. $M_{\rm cloud}$ from CO(3−2) is consistent with these limits (Table 3).

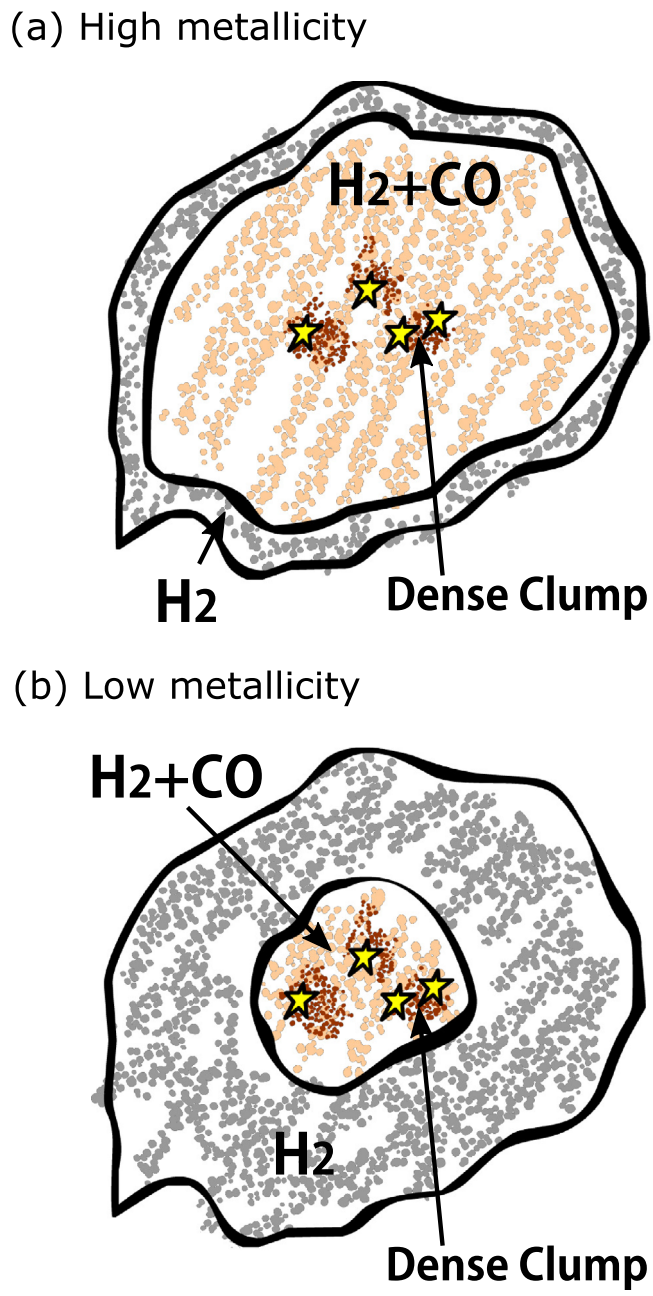

Figure 8. Schematic illustrations of the physical and chemical structures of a molecular cloud (a) in a high-metallicity environment and (b) in a low-metallicity environment. The physical structures (i.e., mass distribution and SF activity) are common between (a) and (b), but their chemical structures (i.e., CO abundances) are different. The ambient radiation penetrates into the cloud, dissociates CO molecules in the cloud's outer layers, and makes them CO-deficient and CO-dark, while more abundant H_2 molecules can self-shield themselves and remain (gray). These CO-dark layers thicken at low metallicity, since a lower dust abundance results in less efficient extinction and allows the radiation to penetrate deeper into the cloud (e.g., Maloney & Black 1988; van Dishoeck & Black 1988). Still, the CO molecules can remain near the cloud center (orange). We hypothesize that the dense clumps (brown), often associated with SF (yellow), are located at the heart of the cloud and likely remain intact with abundant CO molecules. The CO(3−2) emission originates from the dense clump region.

5.4. Star Formation on a 1 kpc Scale

On a 1 kpc scale average, the SF efficiency in total gas content (H I + H_2) is much lower in XUV disks than in the optical disks of nearby galaxies. The average timescale for gas consumption by SF, i.e., the inverse of SF efficiency, is about 2 Gyr in the optical disks (Bigiel et al. 2008; Leroy et al. 2008; see also Kennicutt 1998; Kennicutt & Evans 2012), while it is as long as 100 Gyr over the XUV disk of M83 (Bigiel et al. 2010). As another reference, the gas consumption timescale in the Orion A cloud is about 520 Myr (see Section 3.2 including the caveat on this estimation).

The region of this study is 1 kpc^2 (more accurately, 0.99 kpc^2 by taking into account the round corners of the observed region). The total H I mass in the region is $M_{\rm H\,I} \sim 7.4 \times 10^6\,M_\odot$ from the VLA + GBT data. The total H_2 mass is derived by summing up all the clouds (Table 3) and is $M_{\rm H_2}$ 8.4 $10^4\,M_\odot$, which includes the CO-dark H_2 gas. Only ∼1% of the gas is in the molecular phase. The stellar IMF may not be fully populated in this region of low SF (Koda et al. 2012b). Nevertheless, if we simplistically adopt the standard calibration that assumes a fully populated IMF (Kennicutt & Evans 2012), $L_{\rm H\alpha} \sim 6.8 \times 10^{37}\,{\rm erg\,s^{-1}}$ (Section 3.1) translates to an SFR of $\sim 3.7 \times 10^{-4}\,M_\odot\,{\rm yr^{-1}}$.

The atomic and molecular gas in total, including helium (applying a factor of 1.36 to the mass), would be consumed in about 27 Gyr at this SFR. This is a few times shorter than the average across M83's XUV disk, but is an order of magnitude longer than the average of 2 Gyr in the optical disks and is longer than the Hubble time. On the other hand, the consumption timescale of the molecular gas alone would be as short as 310 Myr, which is similar to that in Orion A (Section 3.2).

Therefore, the molecular clouds in the XUV disk on average appear to be forming stars as much as a typical cloud in the MW, but the XUV disk as a whole is not producing stars as much. This supports the hypothesis that the clouds in the XUV disk and Galactic disk share a similar mass structure, and hence SF activity. The key to the low SF activity in XUV disks should be in the conversion efficiency from the atomic gas to molecular clouds. This is a possibility suggested by Bigiel et al. (2010), and the resolved analysis of the clouds in this study supports it.

5.5. Comparisons to Previous Studies

CO emission was previously detected in the outskirts of four galaxies with XUV disks. Three of them, NGC 4414, NGC 6946, and M63, were observed with a single-dish telescope alone at a relatively low sensitivity and resolution ($\gtrsim 10^{5-6}\,M_\odot$ and ≳300–500 pc, Braine & Herpin 2004; Braine et al. 2007; Dessauges-Zavadsky et al. 2014). If our 1 kpc^2 region in M83 were to be observed at these resolutions, multiple clouds would be in a single telescope beam (Figure 2). A detection in M33 (Braine et al. 2010) was resolved into a single cloud of $\sim 4 \times 10^4\,M_\odot$ with an interferometer (Braine et al. 2012). Our study, together with Braine et al. (2012), demonstrates that high resolution and sensitivity are necessary to identify individual clouds and to investigate the environment of SF in the XUV disks.

There are large-scale CO(1−0) surveys in the outer disk of the MW (e.g., Wouterloot & Brand 1989; Brand & Wouterloot 1994; Digel et al. 1994; Snell et al. 2002; Yang et al. 2002; Brunt et al. 2003; Nakagawa et al. 2005; Sun et al. 2015). The optical edge of the MW disk is around $R_{25} \sim 13.4$ kpc (Goodwin et al. 1997, 1998) with considerable uncertainty due to its edge-on projection. The galactocentric radius of $1.24R_{25}$, corresponding to the 1 kpc^2 region in M83, is $r_{\rm gal} \sim 16.7$ kpc for the MW. The largest, most recent CO survey

by Sun et al. (2015) detected clouds in the far outer MW disk ($r_{\rm gal} \gtrsim 14$ kpc), which include 51 clouds of 10^{2-4} $M_\odot$ in the extreme outer disk ($r_{\rm gal} \gtrsim 16$ up to 21 kpc) with 11 of them at the most massive end of $\gtrsim 10^4$ $M_\odot$. They are spread over a large area of $\sim$80 kpc^2 in Galactic longitude of $l \sim 100°$–$150°$. Therefore, the cloud density is low. The majority are associated with a possible extension of the Scutum–Centaurus spiral arm traced in H I (Sun et al. 2015). SF exists even in the extreme outer disk, but it appears to show mostly low-mass SF (later than B0-type) according to an analysis of the Wide-field Infrared Survey Explorer data (Izumi et al. 2017, see their Figure 15), while much obscured higher-mass SF has yet to be found.

Our 1 kpc^2 region around an H I peak in the XUV disk of M83 has 23 clouds of 10^{3-4} $M_\odot$, including three $\gtrsim 10^4$ $M_\odot$ clouds. Compared to the extreme outer MW disk, the cloud density is high. Obviously, a much larger sample is required to make a general conclusion, but the new detection appears to indicate that molecular clouds, especially their abundance, are one of the key factors for the XUV activity. Figure 6 shows clouds in the inner, outer, and far outer MW disk traced in CO(1−0) (Solomon et al. 1987; Sun et al. 2015, 2017). The XUV clouds in M83, traced in CO(3−2), generally show larger velocity dispersions than the MW clouds. This can be explained if the CO(3−2) emission primarily traces the dense clumps embedded in the clouds (Section 4.3).

6. Implications

6.1. Clouds and Star Formation in XUV Disks

The ALMA CO(3−2) observations constrain the properties of 23 molecular clouds in the XUV disk that have relatively small bulk gas masses of $M_{\rm cloud} = 8.2 \times 10^2$ to 2.3×10^4 $M_\odot$, and dense clump masses of $M_{\rm clump} = 2.7 \times 10^2$ to 7.5×10^3 $M_\odot$. Their ubiquity suggests that these relatively low-mass clouds are a common population of molecular clouds and are the main drivers of the SF activity in the XUV disk.

Numerous previous CO(1−0) and CO(2−1) searches in XUV disks resulted in nondetection (Watson & Koda 2017). A small number of previous detections could not isolate individual clouds due to a combination of low sensitivity and low resolution ($\gtrsim 10^{5-6}$ $M_\odot$ and $\gtrsim$300–500 pc), and one successful case, in the very close galaxy M33, identified only one single cloud of 4.3×10^4 $M_\odot$ (Braine et al. 2012). The common cloud population turns out to be less massive than the previous detections. This study is the first demonstration of the utility of CO(3−2) to detect molecular clouds.

A comparison to Galactic clouds provides insights into the clouds and SF in the XUV disk. For example, a cloud like Orion A—having $M_{\rm cloud} = 4.0 \times 10^4$ $M_\odot$ and $M_{\rm clump} = 7.4 \times 10^3$ $M_\odot$—can be one of the most massive clouds in the observed region. The SF activity in the region, traced by Hα, is also similar to that of the Orion Nebula in Orion A. Orion A is one of the least impressive massive star-forming regions in the MW, but would be the most impressive in the XUV disk. Clouds smaller than Orion A are also found in the XUV disk.

It is likely, and we hypothesize, that the internal mass distributions of molecular clouds are similar in the MW disk and in XUV disks. The Galactic clouds, including Orion A, typically have star-forming dense clumps surrounded by thick layers of bulk molecular gas. In the case of low metallicity of XUV disks, the outer layers should have CO molecules photodissociated and become CO-deficient and CO-dark (Maloney & Black 1988; van Dishoeck & Black 1988; Wolfire et al. 2010). We further hypothesize that the dense clumps at the hearts of the clouds remain intact and maintain a high CO abundance even in the low metallicity (Figure 8). This structure consistently explains the detection of the CO(3−2) emission mainly from the dense clumps, and previous nondetection of the CO(2−1) emission. The common clump–envelope structure between the Galactic and XUV clouds is expected if they are governed primarily by their internal physics (e.g., by self-gravity) independent of their environment. This hypothesis can be tested with future observations, e.g., higher-resolution CO(3−2) observations for resolving the compactness of the clumps, deeper CO(2−1) or CO(1−0) observations for confirming the thermalization, and deeper dust continuum observations for independent mass estimation.

The common mass structure of clouds suggests that average clouds of the same mass should form stars at a similar rate independent of their environment. In other words, the SF efficiency on cloud scales, on average, would be universal. This is supported by the similar gas consumption timescales of the XUV clouds and Orion A.

This study finds only relatively low-mass molecular clouds in the XUV disk of M83. The absence of very bright H II regions in XUV disks may be due to the lack of more massive clouds. Koda et al. (2012b) took the standard stellar initial mass function (Salpeter 1955) as the probability distribution function of stellar mass, and calculated that a star cluster should have a total stellar mass of at least 10^3 $M_\odot$ to populate one 40 $M_\odot$ star (O6 or O7-type; Sternberg et al. 2003). The most massive cloud in our sample has $M_{\rm cloud} = 2.3 \times 10^4$ $M_\odot$, requiring a cloud-to-star mass conversion efficiency of $\sim$4% to produce a 10^3 $M_\odot$ cluster. This is about the efficiency in Galactic molecular clouds (Enoch et al. 2007). The other clouds have even smaller $M_{\rm cloud}$ and are unlikely to form very massive stars and prominent H II regions.

The low SF efficiency on a 1 kpc scale has to originate on scales larger than the clouds; for example, in the conversion efficiency of the extended H I gas into molecular clouds (Bigiel et al. 2010). The mechanism for atomic to molecular gas conversion should also explain the cloud mass function and the lack of massive molecular clouds. Further studies are required to elucidate these aspects, but some clue may already be in the distribution of the CO(3−2) clouds/clumps. The long, chain-like distributions over 600 pc, and potentially the velocity gradient across our field, indicate that their formation is triggered on large scales, such as by large-scale galactic flows.

The hypothesis of the common cloud mass structure (i.e., the clump–envelope structure) in conjunction with the selective photodissociation explains the clouds and SF activity over the optical and XUV disks. This simplistic view could be modified in future studies. For example, this hypothesis exhibits merely an average picture over cloud populations and evolutionary sequences (e.g., see Vázquez-Semadeni et al. 2018). In other extreme environments, such as in the dense Galactic center region, the cloud properties show environmental influences (e.g., Oka et al. 2001) although such regions are relatively small in volume and mass.

6.2. Application to High-z and Other Environments

The common cloud structure (Figure 8) suggests a constant $M_{\rm cloud}/L_{\rm CO(3-2)}$ between high- and low-metallicity environments,

even when CO molecules in cloud outer layers are photodissociated. This has an important implication for CO observations of distant galaxies. The redshifted high-J transitions of CO (higher than $J = 1$ or 2) are often used to trace their total gas mass (Carilli & Walter 2013; Combes 2018). Those high-J CO emissions likely capture only star-forming dense clumps and not the bulk cloud gas. In fact, the CO(1−0) and CO(2−1) luminosities are often beyond those expected from higher-J transition analysis (Carilli et al. 2011; Ivison et al. 2011; Riechers et al. 2011; Bothwell et al. 2013; Daddi et al. 2015). Even then, the high-J CO emissions can trace the total gas mass if the self-gravitating clouds have the same internal structure between the local and distant universe, and if the average ratio of the dense clumps and their parent clouds is about constant independent of environment and redshift, as expected for self-gravitating clouds.

7. Summary

The new ALMA CO(3−2) observations detected a large number of molecular clouds across a 1 kpc^2 area of the XUV disk of M83. Their high abundance suggests that the 23 clouds represent a common population of molecular clouds and are likely the main drivers of the SF activity in XUV disks.

We hypothesized that these clouds share, on average, the same common structure (mass distribution) as Galactic clouds, such as Orion A, and have star-forming dense clumps embedded in thick layers of bulk molecular gas. In the low-metallicity regime of XUV disks, the outer layers of the clouds are likely CO-deficient and CO-dark, while still abundant in H_2, due to selective photodissociation. This hypothesis consistently explains the CO(3−2) detection and CO(2−1) nondetection. The CO(1−0) and CO(2−1) emission should be reduced significantly due to the lack of CO molecules in the photodissociated outer layers where a large fraction of the CO(1−0) and CO(2−1) emission normally originates. The dense clumps have sufficiently high density and temperature for CO(3−2) excitation, reside at the hearts of the clouds, and thus are protected from the dissociation. The common cloud mass structure independent of environment is conceivable if it is governed by their internal physics, e.g., by self-gravity, while their chemical structure could still depend on the environment (e.g., metallicity and radiation field).

The common cloud structure constrains the geometry and physical conditions within molecular clouds, which permits us to estimate their masses. The total masses of the clouds, including the CO-dark H_2 component, range from $M_{\rm cloud} = 8.2 \times 10^2$ to 2.3×10^4 $M_\odot$. Their star-forming dense clumps have masses of $M_{\rm clump} = 2.7 \times 10^2$ to 7.5×10^3 $M_\odot$. The most massive clouds and their dense clumps are similar to Orion A and its dense clump OMC-1. The dense clumps should also radiate CO(2−1) emission, but the flux is lower than the detection limit of the previous CO(2−1) study. This study demonstrates, for the first time, the utility of CO(3−2) emission to find molecular clouds.

The SF activity and efficiency are also similar between the clouds in the XUV disk and Orion A. The XUV disk as a whole shows a much lower SF activity, which is due not to peculiar cloud properties but to the lack of massive clouds. The abundance and mass function of molecular clouds should be regulated by the (unknown) trigger of cloud formation from the abundant atomic gas. Further studies are necessary to elucidate this mechanism, but a clue is already found in the distribution of the clouds. The long chain-like distribution ($\gtrsim$600 pc in length) indicates that the trigger is on large scales.

The common mass structure and SF efficiency among molecular clouds should justify the use of high-J CO transitions as tracers of bulk molecular gas mass in distant galaxies, assuming that the bulk molecular gas mass is proportional to the dense clump mass traced by the high-J transitions.

We thank the referees for useful comments, in particular the first referee for suggesting the discussion in Section 5.5 and the second referee for advice on the title. This paper makes use of the following ALMA data: ADS/JAO.ALMA#2013.1.00861.S and 2017.1.00065.S. ALMA is a partnership of ESO (representing its member states), NSF (USA) and NINS (Japan), together with NRC (Canada), MOST and ASIAA (Taiwan), and KASI (Republic of Korea), in cooperation with the Republic of Chile. The Joint ALMA Observatory is operated by ESO, AUI/NRAO and NAOJ. The Green Bank Observatory and the National Radio Astronomy Observatory are facilities of the National Science Foundation operated under cooperative agreement by Associated Universities, Inc. This research is based in part on data collected at the Subaru Telescope, which is operated by the National Astronomical Observatory of Japan (NAOJ). We are honored and grateful for the opportunity of observing the universe from Maunakea, which has the cultural, historical, and natural significance in Hawaii. Data analysis is in part carried out on the Multi-wavelength Data Analysis System operated by the Astronomy Data Center (ADC) in NAOJ. J.K. acknowledges support from NSF through grants AST-1812847 and AST-2006600 and from NASA grant NNX14AF74G. M.R. wishes to acknowledge support from ANID(CHILE) through FONDECYT grant No1190684.

Facilities: ALMA, Subaru, GBT, VLA, GALEX.

Software: CASA 5.8, GBTIDL, Kapteyn Package, Clumpfind.

ORCID iDs

Jin Koda https://orcid.org/0000-0002-8762-7863
Françoise Combes https://orcid.org/0000-0003-2658-7893
Monica Rubio https://orcid.org/0000-0002-5307-5941
Samuel Boissier https://orcid.org/0000-0002-9091-2366
Masafumi Yagi https://orcid.org/0000-0001-7550-2281
David Thilker https://orcid.org/0000-0002-8528-7340
Amanda M Lee https://orcid.org/0000-0001-8254-6768
Yutaka Komiyama https://orcid.org/0000-0002-3852-6329
Kana Morokuma-Matsui https://orcid.org/0000-0003-3932-0952

References

Alberts, S., Calzetti, D., Dong, H., et al. 2011, ApJ, 731, 28
Asplund, M., Grevesse, N., & Sauval, A. J. 2005, in ASP Conf. Ser. 336, Cosmic Abundances as Records of Stellar Evolution and Nucleosynthesis, ed. I. Barnes, G. Thomas, & F. N. Bash (San Francisco, CA: ASP), 25
Barnes, A. T., Kauffmann, J., Bigiel, F., et al. 2020, MNRAS, 497, 1972
Bergin, E. A., & Tafalla, M. 2007, ARA&A, 45, 339
Bicalho, I. C., Combes, F., Rubio, M., Verdugo, C., & Salome, P. 2019, A&A, 623, A66
Bigiel, F., Leroy, A., Seibert, M., et al. 2010, ApJL, 720, L31
Bigiel, F., Leroy, A., Walter, F., et al. 2008, AJ, 136, 2846
Bolatto, A. D., Leroy, A. K., Rosolowsky, E., Walter, F., & Blitz, L. 2008, ApJ, 686, 948
Bothwell, M. S., Smail, I., Chapman, S. C., et al. 2013, MNRAS, 429, 3047
Braine, J., & Combes, F. 1992, A&A, 264, 433

Braine, J., Ferguson, A. M. N., Bertoldi, F., & Wilson, C. D. 2007, ApJL, 669, L73
Braine, J., Gratier, P., Contreras, Y., Schuster, K. F., & Brouillet, N. 2012, A&A, 548, A52
Braine, J., Gratier, P., Kramer, C., et al. 2010, A&A, 520, A107
Braine, J., & Herpin, F. 2004, Natur, 432, 369
Brand, J., & Wouterloot, J. G. A. 1994, A&AS, 103, 503
Bresolin, F., Ryan-Weber, E., Kennicutt, R. C., & Goddard, Q. 2009, ApJ, 695, 580
Brunt, C. M., Kerton, C. R., & Pomerleau, C. 2003, ApJS, 144, 47
Carilli, C. L., Hodge, J., Walter, F., et al. 2011, ApJL, 739, L33
Carilli, C. L., & Walter, F. 2013, ARA&A, 51, 105
Chambers, K. C., Magnier, E. A., Metcalfe, N., et al. 2016, arXiv:1612.05560
Combes, F. 2018, A&ARv, 26, 5
Daddi, E., Dannerbauer, H., Liu, D., et al. 2015, A&A, 577, A46
Dame, T. M., Ungerechts, H., Cohen, R. S., et al. 1987, ApJ, 322, 706
de Vaucouleurs, G., de Vaucouleurs, A., Corwin, H. G., Jr., et al. 1991, Third Reference Catalogue of Bright Galaxies (New York: Springer)
Dessauges-Zavadsky, M., Verdugo, C., Combes, F., & Pfenniger, D. 2014, A&A, 566, A147
Digel, S., de Geus, E., & Thaddeus, P. 1994, ApJ, 422, 92
Dong, H., Calzetti, D., Regan, M., et al. 2008, AJ, 136, 479
Enoch, M. L., Evans, N. J., II, Sargent, A. I., et al. 2008, ApJ, 684, 1240
Enoch, M. L., Glenn, J., Evans, N. J., II, et al. 2007, ApJ, 666, 982
Fukui, Y., Kawamura, A., Minamidani, T., et al. 2008, ApJS, 178, 56
Gil de Paz, A., Boissier, S., Madore, B. F., et al. 2007a, ApJS, 173, 185
Gil de Paz, A., Madore, B. F., Boissier, S., et al. 2005, ApJL, 627, L29
Gil de Paz, A., Madore, B. F., Boissier, S., et al. 2007b, ApJ, 661, 115
Goodwin, S. P., Gribbin, J., & Hendry, M. A. 1997, AJ, 114, 2212
Goodwin, S. P., Gribbin, J., & Hendry, M. A. 1998, Obs, 118, 201
Großschedl, J. E., Alves, J., Teixeira, P. S., et al. 2019, A&A, 622, A149
Hasegawa, T. 1997, in IAU Symp. 170, CO: Twenty-Five Years of Millimetre-Wave Spectroscopy, ed. W. B. Latter et al. (San Francisco, CA: ASP), 39
Hillenbrand, L. A. 1997, AJ, 113, 1733
Ikeda, M., Maezawa, H., Ito, T., et al. 1999, ApJL, 527, L59
Israel, F. P. 1997, A&A, 328, 471
Ivison, R. J., Papadopoulos, P. P., Smail, I., et al. 2011, MNRAS, 412, 1913
Izumi, N., Kobayashi, N., Yasui, C., Saito, M., & Hamano, S. 2017, AJ, 154, 163
Kennicutt, R. C., & Evans, N. J. 2012, ARA&A, 50, 531
Kennicutt, R. C., Jr. 1998, ARA&A, 36, 189
Koda, J., Sawada, T., Sakamoto, K., et al. 2020, ApJL, 890, L10
Koda, J., Scoville, N., Hasegawa, T., et al. 2012a, ApJ, 761, 41
Koda, J., Yagi, M., Boissier, S., et al. 2012b, ApJ, 749, 20
Komugi, S., Kohno, K., Tosaki, T., et al. 2007, PASJ, 59, 55
Kong, S., Arce, H. G., Feddersen, J. R., et al. 2018, ApJS, 236, 25
Lemonias, J. J., Schiminovich, D., Thilker, D., et al. 2011, ApJ, 733, 74
Leroy, A. K., Rosolowsky, E., Usero, A., et al. 2022, ApJ, 927, 149
Leroy, A. K., Walter, F., Brinks, E., et al. 2008, AJ, 136, 2782
Maloney, P., & Black, J. H. 1988, ApJ, 325, 389
Masui, S., Yamasaki, Y., Ogawa, H., et al. 2021, PASJ, 73, 1100
McMullin, J. P., Waters, B., Schiebel, D., Young, W., & Golap, K. 2007, in ASP Conf. Ser. 376, Astronomical Data Analysis Software and Systems XVI, ed. R. A. Shaw, F. Hill, & D. J. Bell (San Francisco, CA: ASP), 127
Miura, R. E., Kohno, K., Tosaki, T., et al. 2012, ApJ, 761, 37
Miura, R. E., Kohno, K., Tosaki, T., et al. 2014, ApJ, 788, 167
Morokuma-Matsui, K., & Muraoka, K. 2017, ApJ, 837, 137
Nakagawa, M., Onishi, T., Mizuno, A., & Fukui, Y. 2005, PASJ, 57, 917
Nakamura, F., Ishii, S., Dobashi, K., et al. 2019, PASJ, 71, S3
Nakamura, T., Kodaira, S., Ishii, K., Inatani, J., & Ohishi, M. 1984, PASJ, 36, 123
Oka, T., Hasegawa, T., Sato, F., et al. 2001, ApJ, 562, 348
Onodera, S., Kuno, N., Tosaki, T., et al. 2012, PASJ, 64, 133
Pabst, C. H. M., Hacar, A., Goicoechea, J. R., et al. 2021, A&A, 651, A111
Pak, S., Jaffe, D. T., van Dishoeck, E. F., Johansson, L. E. B., & Booth, R. S. 1998, ApJ, 498, 735
Planck Collaboration, Ade, P. A. R., Aghanim, N., et al. 2011, A&A, 536, A19
Riechers, D. A., Hodge, J., Walter, F., Carilli, C. L., & Bertoldi, F. 2011, ApJL, 739, L31
Rubio, M., Elmegreen, B. G., Hunter, D. A., et al. 2015, Natur, 525, 218
Sakamoto, S., Hayashi, M., Hasegawa, T., Handa, T., & Oka, T. 1994, ApJ, 425, 641
Salpeter, E. E. 1955, ApJ, 121, 161
Schraml, J., & Mezger, P. G. 1969, ApJ, 156, 269
Scoville, N., Sheth, K., Aussel, H., et al. 2016, ApJ, 820, 83
Scoville, N. Z., Polletta, M., Ewald, S., et al. 2001, AJ, 122, 3017
Scoville, N. Z., & Sanders, D. B. 1987, in Interstellar Processes, ed. D. J. Hollenbach & H. A. Thronson, Jr. (Dordrecht: Reidel Publishing), 21
Simón-Díaz, S., García-Rojas, J., Esteban, C., et al. 2011, A&A, 530, A57
Snell, R. L., Carpenter, J. M., & Heyer, M. H. 2002, ApJ, 578, 229
Solomon, P. M., Rivolo, A. R., Barrett, J., & Yahil, A. 1987, ApJ, 319, 730
Sorai, K., Hasegawa, T., Booth, R. S., et al. 2001, ApJ, 551, 794
Sternberg, A., Hoffmann, T. L., & Pauldrach, A. W. A. 2003, ApJ, 599, 1333
Sun, Y., Su, Y., Zhang, S.-B., et al. 2017, ApJS, 230, 17
Sun, Y., Xu, Y., Yang, J., et al. 2015, ApJL, 798, L27
Thilker, D. A., Bianchi, L., Boissier, S., et al. 2005, ApJL, 619, L79
Thilker, D. A., Bianchi, L., Meurer, G., et al. 2007, ApJS, 173, 538
Thim, F., Tammann, G. A., Saha, A., et al. 2003, ApJ, 590, 256
van Dishoeck, E. F., & Black, J. H. 1988, ApJ, 334, 771
Vázquez-Semadeni, E., Zamora-Avilés, M., Galván-Madrid, R., & Forbrich, J. 2018, MNRAS, 479, 3254
Vlahakis, C., van der Werf, P., Israel, F. P., & Tilanus, R. P. J. 2013, MNRAS, 433, 1837
Walter, F., Brinks, E., de Blok, W. J. G., et al. 2008, AJ, 136, 2563
Watanabe, Y., Nishimura, Y., Harada, N., et al. 2017, ApJ, 845, 116
Watson, L. C., & Koda, J. 2017, in Outskirts of Galaxies, ed. J. H. Knapen, J. C. Lee, & A. Gil de Paz, Vol. 434 (New York: Springer International), 175
Watson, L. C., Martini, P., Lisenfeld, U., Böker, T., & Schinnerer, E. 2016, MNRAS, 455, 1807
Westerlund, B. E. 1997, The Magellanic Clouds (Cambridge: Cambridge Univ. Press)
Williams, J. P., de Geus, E. J., & Blitz, L. 1994, ApJ, 428, 693
Wilson, C. D., Warren, B. E., Israel, F. P., et al. 2009, ApJ, 693, 1736
Wolfire, M. G., Hollenbach, D., & McKee, C. F. 2010, ApJ, 716, 1191
Wong, T., Hughes, A., Ott, J., et al. 2011, ApJS, 197, 16
Wouterloot, J. G. A., & Brand, J. 1989, A&AS, 80, 149
Yagi, M., Suzuki, N., Yamanoi, H., et al. 2013, PASJ, 65, 22
Yagi, M., Yoshida, M., Gavazzi, G., et al. 2017, ApJ, 839, 65
Yang, J., Jiang, Z., Wang, M., Ju, B., & Wang, H. 2002, ApJS, 141, 157